Inorganic Chemistry

ARTICLE

pubs.acs.org/IC

Complete Family of Mono-, Bi-, and Trinuclear $Re^{I}(CO)_3Cl$ Complexes of the Bridging Polypyridyl Ligand 2,3,8,9,14,15-Hexamethyl-5,6,11,12,17,18-hexaazatrinapthalene: Syn/Anti Isomer Separation, Characterization, and Photophysics

Michael G. Fraser,[†] Charlotte A. Clark,[‡] Raphael Horvath,[†] Samuel J. Lind,[†] Allan G. Blackman,[†] Xue-Zhong Sun,[‡] Michael W. George,[*,‡] and Keith C. Gordon[*,†]

[†]MacDiarmid Institute for Advanced Materials and Nanotechnology, Department of Chemistry, University of Otago, Dunedin, New Zealand

[‡]School of Chemistry, University of Nottingham, Nottingham NG7 2RD, United Kingdom

Supporting Information

ABSTRACT: The syn and anti isomers of the bi- and trinuclear $Re(CO)_3Cl$ complexes of 2,3,8,9,14,15-hexamethyl-5,6,11,12,17,18-hexaazatrinapthalene (HATN-Me_6) are reported. The isomers are characterized by ^1H NMR spectroscopy and X-ray crystallography. The formation of the binuclear complex from the reaction of HATN-Me_6 with 2 equiv of $Re(CO)_5Cl$ in chloroform results in a 1:1 ratio of the syn and anti isomers. However, synthesis of the trinuclear complex from the reaction of HATN-Me_6 with 3 equiv of $Re(CO)_5Cl$ in chloroform produces only the anti isomer. *syn*-{$(Re(CO)_3Cl)_3(\mu$-HATN-$Me_6)$} can be synthesized by reacting 1 equiv of $Re(CO)_5Cl$ with *syn*-{$(Re(CO)_3Cl)_2(\mu$-HATN-$Me_6)$} in refluxing toluene. The product is isolated by subsequent chromatography. The X-ray crystal structures of *syn*-{$(Re(CO)_3Cl)_2(\mu$-HATN-$Me_6)$} and *anti*-{$(Re(CO)_3Cl)_3(\mu$-HATN-$Me_6)$} are presented both showing severe distortions of the HATN ligand unit and intermolecular π stacking. The complexes show intense absorptions in the visible region, comprising strong $\pi \rightarrow \pi^*$ and metal-to-ligand charge-transfer (MLCT) transitions, which are modeled using time-dependent density functional theory (TD-DFT). The energy of the MLCT absorption decreases from mono- to bi- to trinuclear complexes. The first reduction potentials of the complexes become more positive upon binding of subsequent $Re(CO)_3Cl$ fragments, consistent with changes in the energy of the MLCT bands and lowering of the energy of relevant lowest unoccupied molecular orbitals, and this is supported by TD-DFT. The nature of the excited states of all of the complexes is also studied using both resonance Raman and picosecond time-resolved IR spectroscopy, where it is shown that MLCT excitation results in the oxidation of one rhenium center. The patterns of the shifts in the carbonyl bands upon excitation reveal that the MLCT state is localized on one rhenium center on the IR time scale.

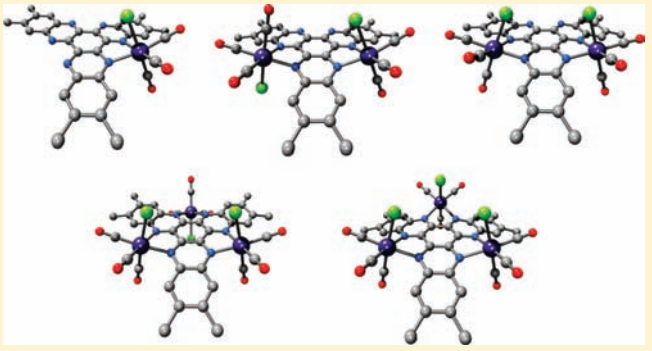

INTRODUCTION

Materials based on hexaazatrinapthalene (HATN) are of considerable interest for a number of reasons. First, HATN ligands are able to self-organize into discotic liquid crystals that may transport charge.[1−5] Second, HATN can readily store negative charge, thereby allowing the material to be used as an n-type carrier in blended electroluminescent organic semiconductor devices.[6] The use of HATN-type compounds in the formation of columnar structures with nanometer dimensions has also been studied.[7] The properties of these compounds may be further exploited by using the ligating properties of HATN; it is a tris-bidentate ligand capable of accommodating up to three metals.

There is a rich coordination chemistry associated with the related 1,4,5,8,9,12-hexaazatriphenylene (HAT) ligand.[8] One of the drivers for this is the creation of photoadducts from the interactions of $[Ru(bpy)(HAT)_2]^{2+}$ (bpy = 2,2′-bipyridine) and similar compounds with G-rich nucleotides as a method of "gene-silencing".[9] The first report of a HATN metal complex was by Gray et al.[10] They recognized that HATN-type ligands are easier to synthesize than HAT, and in this study, the ligand 2,3,8,9,14,15-hexamethyl-5,6,11,12,17,18-hexaazatrinapthalene (HATN-Me_6) was used to form mono- and binuclear complexes with $\{PdCl_2\}$ and $\{Re(CO)_3Cl\}$ moieties. The binuclear complexes $(PdCl_2)_2(\mu$-HATN-$Me_6)$ and $(PdCl_2)(\mu$-HATN-$Me_6)$-$(Re(CO)_3Cl)$ were reported, while the crystal structures of

Received: January 24, 2011
Published: June 03, 2011

Scheme 1. Synthesis of Compounds in This Study Including Ratios of Starting Materials (Ligand: Metal Fragment) and the Solvent Used in the Reaction

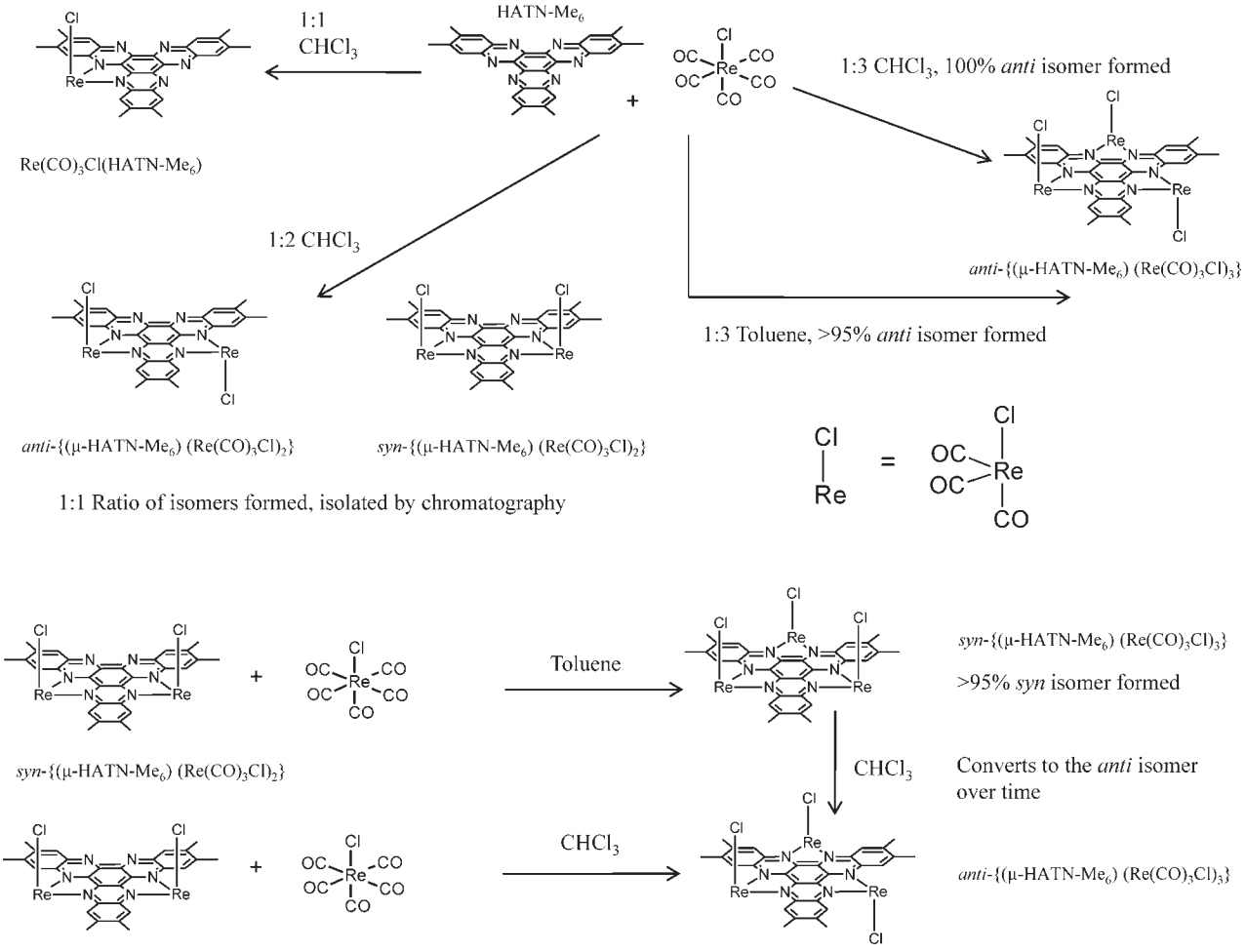

the mononuclear complexes $(Re(CO)_3Cl)(HATN\text{-}Me_6)$ and $(PdCl_2)(HATN\text{-}Me_6)$ and the heterobinuclear complex $(PdCl_2)(\mu\text{-}HATN\text{-}Me_6)(Re(CO)_3Cl)$ were presented in this work. McKeown et al.[11] also showed that three $\{PdCl_2\}$ units can be bound to a HATN ligand within a HATN-based network polymer.

The electrochemical properties of a number of trinuclear $\{(Ru(acac)_2)_3HATN\}$ complexes have been investigated by Kaim et al.[12,13] They found that the complexes displayed three successive reversible one-electron reductions (ligand-based) and three successive reversible one-electron oxidations (metal-based). Their studies using HATN, HATN-Me_6, and HATN-Cl_6 showed that the comproportionation constants (K_c) for the $Ru_3^{III,II,II}$ and $Ru_3^{III,III,II}$ complexes ranged from 10^4 to 10^8, indicating a reasonable level of intermetal coupling; this was supported by density functional theory (DFT) calculations on the compounds. It was noted that no intravalence charge-transfer transitions could be detected, and this observation was attributed to the 3-fold symmetry of the trinuclear complexes.[12] In addition, no mono- or binuclear complexes could be isolated.[13]

The reaction of copper(I) starting materials with HATN ligands also appears to only give trinuclear products. For example, the reaction of $[Cu(PPh_3)_4](BF_4)$ with HATN-Me_6 in ether gives $[(Cu(PPh_3)_2)_3(\mu\text{-}HATN\text{-}Me_6)](BF_4)_3$, the crystal structure of which has been reported along with analysis of the optical spectra using DFT and resonance Raman (RR) excitation profiles.[14] The crystal structure reveals that binding of the metal unit results in small but significant twisting of the aromatic HATN-Me_6 unit in the complex. The Cu^I ion shows a typical distorted tetrahedral geometry, with small N−Cu−N bond angles of around 80° and triphenylphosphine P−Cu−P angles ranging from 115° to 125°. The $\pi \rightarrow \pi^*$ transition present at 410 nm in the free HATN-Me_6 ligand is red-shifted to 430 nm in the $[(Cu(PPh_3)_2)_3(\mu\text{-}HATN\text{-}Me_6)](BF_4)_3$ complex, which also displays a metal-to-ligand charge-transfer (MLCT) band at 590 nm.

A study of the electrochemical properties of the trinuclear copper(I) complex $[(Cu(dppf))_3(\mu\text{-}HATN)]^{3+}$ [dppf = 1,1-bis(diphenylphosphino)ferrocene] reveals that oxidation of this species by up to three electrons is possible, and two reductions may also be observed.[15] The crystal structure of $[(Cu(dppf))_3(\mu\text{-}HATN)](BF_4)_3$ shows an inequivalence of the six Cu−N bond lengths, leading to notable deviation from 3-fold symmetry, and the structure also shows the close association of two tetrafluoroborate anions to the cation.

The *fac*-$\{Re(CO)_3Cl\}$ unit has been well utilized in inorganic photochemistry. Rhenium(I) polypyridyl complexes of the type *fac*-$\{Re(CO)_3(NN)L\}$, where NN = a bidentate polypyridyl

dx.doi.org/10.1021/ic200136t |*Inorg. Chem.* 2011, 50, 6093–6106

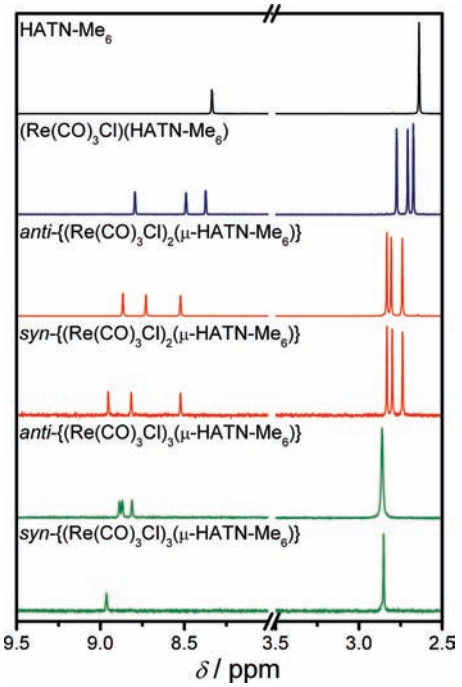

Figure 1. Aromatic and methyl group regions of the ^{1}H NMR spectra (400 MHz, $CDCl_3$, 298 K) of the compounds in this study. All spectra are referenced to the residual $CDCl_3$ peak at 7.26 ppm.

ligand and L = a halide or nitrogen-donor ligand, are a well-studied class of compounds because of their rich photophysical properties.[16] These properties have led to the investigation of such compounds for use in dye-sensitized solar cells,[17] CO_2 sequestration,[18,19] biological probes[20,21] and molecular electronics, including light-emitting diodes.[22−29] The $\{Re(CO)_3Cl\}$ fragment can be manipulated, primarily through substitution of the chloride ion, to build structures such as oligomers[30] and cages.[31]

In a recent study,[32] Kubiak et al. reported the synthesis and characterization of the mononuclear $(Re(CO)_3Cl)$(HATN) complex and a binuclear complex of HATN-Me_6, $\{(Re(CO)_3Cl)_2(\mu$-HATN-$Me_6)\}$, where the two chloride atoms were found to lie on the same side of the ligand plane, i.e., the syn isomer.

In this study, we present the separation of the syn and anti isomers (Scheme 1) of binuclear $\{(Re(CO)_3Cl)_2(\mu$-HATN-$Me_6)\}$ and also trinuclear $\{(Re(CO)_3Cl)_3(\mu$-HATN-$Me_6)\}$ complexes. To our knowledge, this is the first example of $Re^I(CO)_3Cl$ polypyridyl complexes where both the syn and anti isomers have been synthesized and subsequently separated. The isomers may be differentiated by their ^{1}H NMR spectra, separated by column chromatography, and assigned by X-ray crystallography.

We also present the electronic properties of the complexes, investigated using cyclic voltammetry and UV−vis absorption spectroscopy, in concert with time-dependent DFT (TD-DFT) calculations. Also investigated are the excited-state properties, using RR spectroscopy and time-resolved IR spectroscopy (TRIR). The complexes show intense absorptions in the visible region, comprising strong $\pi \rightarrow \pi^*$ and MLCT transitions. The RR spectra of the carbonyl bands reveal coupling between $\{Re(CO)_3Cl\}$ fragments. TRIR experiments confirm the lowest excited state in these complexes to be MLCT in character, with lifetimes that vary depending of the number of $\{Re(CO)_3Cl\}$ centers.

RESULTS AND DISCUSSION

2.1. Synthesis and Isomer Separation. The methods for the synthesis of HATN complexes in this study are shown in Scheme 1. $\{(Re(CO)_3Cl)_2(\mu$-HATN-$Me_6)\}$ was prepared by refluxing 2 equiv of $Re(CO)_5Cl$ with HATN-Me_6 in chloroform. Initially, the presence of isomers was confirmed by the ^{1}H NMR spectrum of the crude material and also thin-layer chromatography (bands with R_f = 0.5 and 0.2 were observed). Subsequent column chromatography on silica gel (CH_2Cl_2/ethyl acetate 5%) resulted in separation of the two species. Microanalysis and mass spectra of the separated fractions confirmed that the species had the same molecular formula but different ^{1}H NMR spectra, which were attributed to syn and anti isomers. Figure 1 shows the two ^{1}H NMR spectra of the separated isomers. The three signals due to the methyl groups, which range between 2.74 and 2.83 ppm, are very similar between the two isomers. However, while both isomers share an aromatic peak at the same chemical shift (8.59 ppm), two of the three peaks assigned to the aromatic protons are at different chemical shifts. The similarity of the chemical shifts of the methyl groups but differences between those of the aromatic protons between isomers can be attributed to the fact that the aromatic protons are much closer to the $\{Re(CO)_3Cl\}$ moieties than the methyl protons and, hence, are in unique environments in each isomer. The aromatic peak common to both isomers can be assigned to the protons pointing into the uncoordinated binding pocket of each complex. The isomer ratio was approximately 1:1. Assignment of the isomers was confirmed by X-ray crystallography, where crystals of suitable quality from the species with an R_f = 0.2 were grown by vapor diffusion of hexane into a concentrated chloroform solution. This was shown to be the syn isomer (vide infra), leaving the species R_f = 0.5 assigned as the anti isomer.

The reaction of $Re(CO)_5Cl$ with HATN-Me_6 in a 3:1 ratio in chloroform results in a single product. Figure 1 shows the ^{1}H NMR spectrum of the crude material. In this, the methyl protons appear as a single peak, as is the case in the free ligand. However, three signals are observed for the aromatic protons, indicating that each proton is in a unique environment. This product is the anti isomer of $\{(Re(CO)_3Cl)_3(\mu$-HATN-$Me_6)\}$, as confirmed by X-ray crystallography (vide infra). As in the case of the two binuclear isomers, the chemical shifts of the aromatic protons are affected by the relative orientations of the Re−Cl moieties, whereas the shifts of the methyl groups are not. In the binuclear case, the ratio of the isomers formed is approximately 1:1. For the trinuclear complex, when chloroform is used as a solvent, the anti isomer is formed exclusively rather than the statistically expected 3:1 anti/syn ratio. However, the reaction of 3 equiv of $Re(CO)_5Cl$ with HATN-Me_6 in toluene rather than chloroform resulted in a mixture of products, including a small amount (~5%) of the *syn*-$\{(Re(CO)_3Cl)_3(\mu$-HATN-$Me_6)\}$ complex. This isomer is distinguished by its ^{1}H NMR spectrum, which consists of a single aromatic peak and a single methyl peak (Figure 1). It was not possible to isolate *syn*-$\{(Re(CO)_3Cl)_3(\mu$-HATN-$Me_6)\}$ from this reaction mixture. The syn isomer was therefore isolated by using the alternate synthetic strategy of reacting the binuclear *syn*-$\{(Re(CO)_3Cl)_2(\mu$-HATN-$Me_6)\}$ with 1 equiv of $Re(CO)_5Cl$ in toluene. One might expect this reaction to give a 1:1 ratio of *syn*- and *anti*-$\{(Re(CO)_3Cl)_3(\mu$-HATN-$Me_6)\}$. However, in this solvent, the desired trinuclear syn isomer is obtained in >95% yield relative to the anti isomer and can be obtained pure following column

dx.doi.org/10.1021/ic200136t |*Inorg. Chem.* 2011, 50, 6093–6106

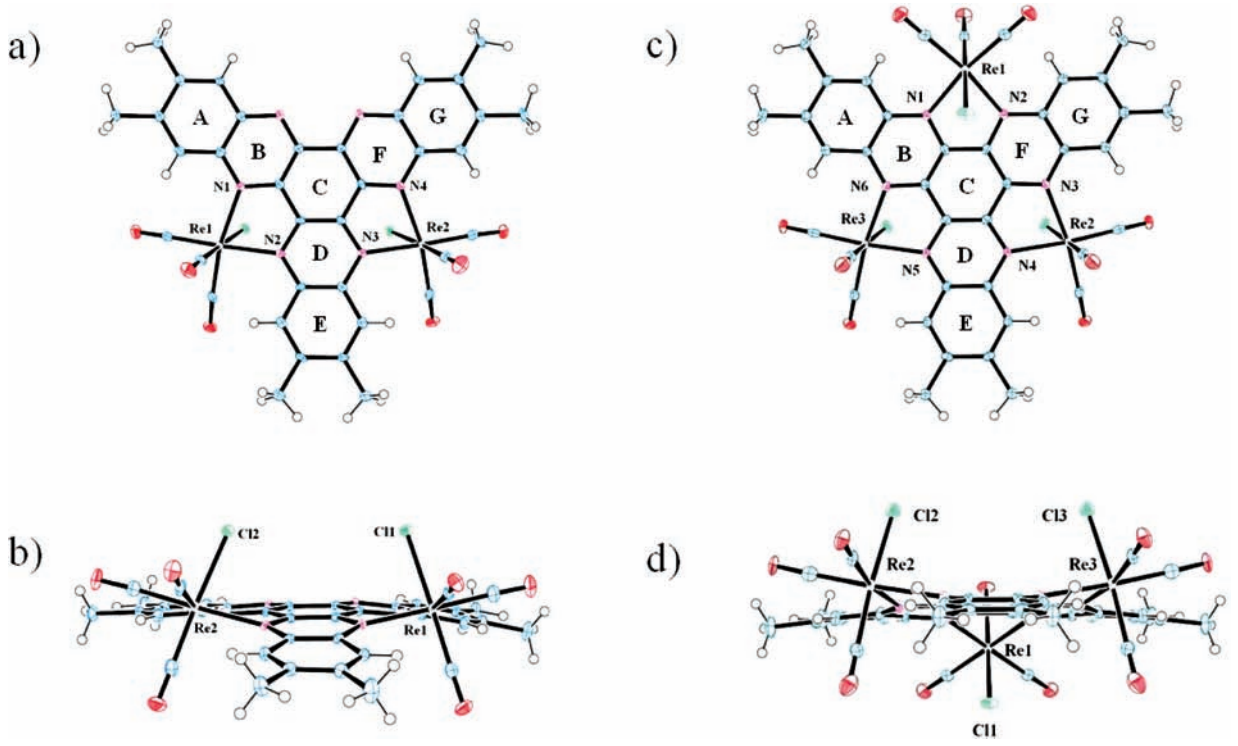

Figure 2. X-ray crystal structures of *syn*-{$(Re(CO)_3Cl)_2(\mu$-HATN-$Me_6)$} (a and b) and *anti*-{$(Re(CO)_3Cl)_3(\mu$-HATN-$Me_6)$} (c and d). Ellipsoids are drawn at the 50% probability level.

chromatography. When the reaction between *syn*-{$(Re(CO)_3Cl)_2(\mu$-HATN-$Me_6)$} and $Re(CO)_5Cl$ is carried out in chloroform, the product obtained is *anti*-{$(Re(CO)_3Cl)_3(\mu$-HATN-$Me_6)$} in almost quantitative yield. This is unsurprising because the reaction of 3 equiv of $Re(CO)_5Cl$ with HATN-Me_6 in chloroform also results in a 100% yield of the anti isomer.

As is the case in the binuclear compounds, the syn and anti isomers of {$(Re(CO)_3Cl)_3(\mu$-HATN-$Me_6)$} have different solubilities in common organic solvents. In particular, the syn isomer is much less soluble than the anti isomer in chlorinated solvents. All of the complexes in this study appear to be stable in solution at room temperature, with the exception of the *syn*-{$(Re(CO)_3Cl)_3(\mu$-HATN-$Me_6)$} complex. This complex converts to the trinuclear anti isomer over time in chloroform, dichloromethane, and acetone, although it is stable in a toluene solution. The ^{1}H NMR spectra over time of a solution of *syn*-{$(Re(CO)_3Cl)_3(\mu$-HATN-$Me_6)$} at room temperature in $CDCl_3$ show no peaks due to the anti isomer over 24 h. However, over 5 days under these conditions, the syn isomer converts completely to the anti isomer. This isomerization process must presumably involve Re−N cleavage, and such kinetic lability of the $Re(CO)_3Cl$ fragment is unusual.[16] This instability of *syn*-{$(Re(CO)_3Cl)_3(\mu$-HATN-$Me_6)$} in a chloroform solution may, in part, be the reason why the reaction of 3 equiv of $Re(CO)_5Cl$ with HATN-Me_6 in refluxing chloroform results exclusively in the anti isomer. As a result of this instability, all spectroscopic measurements on *syn*-{$(Re(CO)_3Cl)_3(\mu$-HATN-$Me_6)$} were performed on solutions made up immediately prior to data collection.

The use of chloroform as the solvent in these synthetic reactions has proven very useful; traditionally, toluene has been used,[10,32] and the trinuclear complexes have hitherto not been reported. Also, both syn and anti isomers of the binuclear complexes could not be characterized when toluene was used as the solvent.

2.2. Structural Characterization. Assignment of the binuclear isomers was achieved by X-ray crystallography, where crystals from the second fraction (R_f = 0.2) were grown by diffusion of hexane into a concentrated chloroform solution. The structure was shown to be that of the syn isomer (Figure 2a,b).

Kubiak et al.[32] recently published a crystal structure of a different polymorph of *syn*-{$(Re(CO)_3Cl)_2(\mu$-HATN-$Me_6)$}, obtained using crystals also grown from hexane and chloroform. The unit cell they presented contains four chloroform solvent molecules, and the molecules show no intermolecular $\pi-\pi$ stacking.

The crystallographic and structural refinement data for both structures in this study are shown in Table S1 in the Supporting Information. *syn*-{$(Re(CO)_3Cl)_2(\mu$-HATN-$Me_6)$} crystallizes in the monoclinic space group $P2_1/n$. The unit cell comprises four complex molecules and eight chloroform molecules. A significant difference between the structure we present and that of Kubiak et al. is the intermolecular $\pi-\pi$ stacking that we observe between the complexes (Figure S1 in the Supporting Information).

The structure of the *syn*-{$(Re(CO)_3Cl)_2(\mu$-HATN-$Me_6)$} complex displays some differences compared to that of the free HATN-Me_6 ligand.[33] The central benzene ring shows the most significant changes, with an average shortening of the C−C bonds upon complexation of 0.024 Å. The entire HATN-Me_6 aromatic unit is nonplanar, similar to the distortion observed in the mononuclear $(Re(CO)_3Cl)$(HATN-Me_6) case. The mean planes of the pyrazine rings B, D, and F (Figure 2) are at angles of 6.37°, 4.05°, and 6.89°, respectively, to a mean plane through the central ring (ring C). This is in comparison to the free ligand with angles of 0.85° and 1.03° between the central and pyrazine rings, respectively. While the free ligand displays angles ranging from

dx.doi.org/10.1021/ic200136t |*Inorg. Chem.* 2011, 50, 6093–6106

1.60° to 1.68° between the central phenyl ring mean plane and those of the outer phenyl rings, in the complex these angles are 10.7°, 3.53°, and 11.87° for the A, G, and E rings, respectively, showing that the ligand is twisted asymmetrically. This asymmetry is also reflected by the fact that the two Re atoms lie beneath the mean plane of the central ring by differing amounts: Re1, 0.3476 Å; Re2, 0.4669 Å. Both rhenium centers display distorted octahedral coordination environments, with N−Re−N bite angles of 75.52° and 75.16° for Re1 and Re2, respectively. All Re−N, Re−C, and Re−Cl bond lengths are within the observed ranges. The experimental distortions are also predicted in the calculated structure of *syn*-{$(Re(CO)_3Cl)_2(\mu$-HATN-$Me_6)$} in which the mean planes of the pyrazine rings B, D, and F lie at angles of 3.62°, 7.66°, and 3.61°, respectively, to the central ring (ring C). Also, the rhenium metal centers are calculated at 0.462 Å beneath the mean plane of the central ring.

Within the unit cell, two complexes dimerize via $\pi-\pi$ stacking through the outer phenyl rings (Figure S1 in the Supporting Information). Centroid-to-plane distances of 3.483 and 3.505 Å and a centroid-to-centroid distance of 3.594 Å are within typical values for $\pi-\pi$ interactions.[34] The result is that the nonbinding nitrogen pockets stack close to each other (intermolecular N6−N5: 3.075 Å). The two syn chloride ligands fit into this open site, allowing stacking between complementary A and G rings. The large {$Re(CO)_3Cl$} fragment hinders any $\pi-\pi$ interactions between other sections of the molecule.

In the case of the trinuclear complexes, the syn and anti isomers can be assigned from their distinct ^{1}H NMR signals. The structure of *anti*-{$(Re(CO)_3Cl)_3(\mu$-HATN-$Me_6)$} was confirmed by X-ray crystallography, where crystals of suitable quality were grown by diffusion of hexane into a CH_2Cl_2 solution. Parts c and d of Figure 2 show two views of *anti*-{$(Re(CO)_3Cl)_3(\mu$-HATN-$Me_6)$}. As is also found in *syn*-{$(Re(CO)_3Cl)_2(\mu$-HATN-$Me_6)$}, the aromatic HATN-Me_6 unit is significantly bent, with angles between the mean plane of the central phenyl ring (C) and mean planes of the outer rings (A, E, and G) of 7.59° for rings A and G and 15.33° for ring E.

Similar distortions of the HATN ligand upon complexation have been seen in the few other crystallographically characterized complexes containing three metal ions bound to HATN-Me_6 but not to the extent of that seen in this case. For example, the mean-plane angles between the central and outer ring mean planes are 6.93° in $[(Cu(PPh_3)_2)_3(\mu$-HATN-$Me_6)](BF_4)_3$,[14] while smaller distortions are seen in both $[(Cu(dppf))_3(\mu$-HATN$)](BF_4)_3$[15] and {$(TiCp_2)_3(\mu$-HATN-$Me_6)$}.[35] Silver(I) coordination polymers of HATN[36] also show much less distortion of the HATN ligand compared to complexes containing the {$Re(CO)_3Cl$} moiety.

The side-on view of *anti*-{$(Re(CO)_3Cl)_3(\mu$-HATN-$Me_6)$} (Figure 2d) emphasizes the anti disposition of the chloride ligands. One of the striking features of this structure is the severely distorted octahedral geometry of the unique {$Re(CO)_3Cl$} moiety, labeled Re1 in Figure 2c,d. The two syn rhenium centers are symmetry related, and both sit 0.306 Å above the plane of the central aromatic ring, with the anti rhenium center sitting 0.766 Å below the plane. This is also borne out in the calculated structures with the anti rhenium center calculated 0.718 Å below the plane and the two syn rhenium centers 0.518 Å above the plane of the central aromatic ring. The distortion of the ligand moiety is also predicted in the calculated structure, with the angles between the mean plane of the central phenyl ring (C) and mean planes of the outer rings (A, E, and G) of 3.65° for rings A and G and 14.08° for ring E.

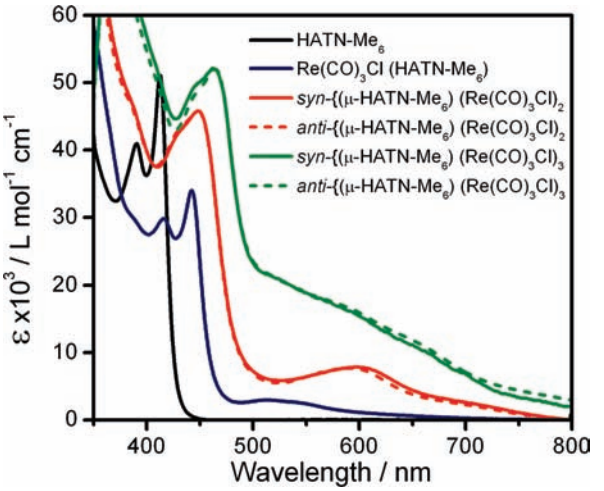

Figure 3. Electronic absorption spectra of the HATN-Me_6 ligand and the respective rhenium complexes. Spectra were obtained in CH_2Cl_2.

Another example of this is the angle of the plane through the rhenium ion and the equatorial carbonyl ligands relative to the plane through the N1−C−C−N2 atoms (i.e., the equatorial coordination planes). This angle is 33.19°, and the analogous angles of the two *syn*-{$Re(CO)_3Cl$} moieties are 22.78°. Similar but less severe distortions have been observed previously in {$Re(CO)_3Cl$} polypyridyl complexes,[37−40] possibly, in part, because of the destabilizing steric interactions between the equatorial carbonyl ligands and the protons on the pyridyl ligand ortho to the nitrogen-donor atoms.[41]

The trinuclear complex stacks through intermolecular $\pi-\pi$ interactions in a fashion similar to that observed in *syn*-{$(Re(CO)_3Cl)_2(\mu$-HATN-$Me_6)$} (Figure S1 in the Supporting Information). The outer phenyl rings of two complementary molecules have centroid-to-centroid distances of 4.166 Å and a centroid-to-plane distance of 3.921 Å. These values are within the range of typical values for $\pi-\pi$ interactions,[34] but the two *anti*-{$(Re(CO)_3Cl)_3(\mu$-HATN-$Me_6)$} molecules are >0.4 Å further apart than the two *syn*-{$(Re(CO)_3Cl)_2(\mu$-HATN-$Me_6)$} molecules in the dimer reported above. This is rather unsurprising because the third anti rhenium chloride fragment perturbs the more intimate stacking that is present in *syn*-{$(Re(CO)_3Cl)_2(\mu$-HATN-$Me_6)$}.

2.3. Electronic Absorption Spectra and TD-DFT Calculations. Figure 3 shows the electronic absorption spectra of the free HATN-Me_6 ligand and the rhenium complexes, and the electronic absorption data are collated in Table 1. The complexes are intensely colored; solid samples appear almost black, dilute solutions of the mononuclear complex are an orange color, and the bi- and trinuclear complexes appear green in color. Solutions of the ligand are orange. HATN-Me_6 shows intense $\pi \rightarrow \pi^*$ absorptions at 394 and 416 nm. The binding of one {$Re(CO)_3Cl$} moiety induces a red shift and a slight broadening of the $\pi \rightarrow \pi^*$ transitions, which now appear at 416 and 444 nm. There is also an additional component of lower intensity at 514 nm, which is assigned as an MLCT transition. The band profile of the lower-energy transition is asymmetric, with a small amount of additional absorbance appearing on the red edge of the band. This implies a further transition of even lower intensity and energy. The spectra of the syn and anti isomers of the binuclear complex are very similar in nature, with only some

dx.doi.org/10.1021/ic200136t |*Inorg. Chem.* 2011, 50, 6093–6106

Table 1. Experimental and Calculated Electronic Transitions of HATN-Me$_6$, (Re(CO)$_3$Cl)(HATN-Me$_6$) (Re1), *syn*- and *anti*-{(Re(CO)$_3$Cl)$_2$(μ-HATN-Me$_6$)} (Re2), and *syn*- and *anti*-{(Re(CO)$_3$Cl)$_3$(μ-HATN-Me$_6$)} (Re3)[a]

	experimental			calculated		
	band energy/nm	extinction coeff/L mol^{-1} cm^{-1}	band assignment	band energy/nm	f	orbital contributions
HATN-Me$_6$	416	51 000	$\pi \rightarrow \pi^*$	383	0.095	H, L (44%); H-1, L (44%)
Re1	444	34 000	$\pi \rightarrow \pi^*$	363	0.090	H-3, L (47%); H-5, L (29%)
	514	2000	MLCT	474	0.040	H-1, L (93%)
				524	0.001	H, L (96%)
Re2	448	45 800	$\pi \rightarrow \pi^*$	379	0.012	H-7, L (76%)
	591	6200	MLCT	539	0.080	H-2, L (69%); H, L (17%)
				606	0.008	H-2, L (−15%); H-1, L+1 (−15%); H, L (68%)
Re3	464	52 000	$\pi \rightarrow \pi^*$	340	0.283	H-21, L (21%); H-11, L+2 (24%); H-22, L (−21%); H-11, L+1 (23%)
	602	16 000	MLCT	446	0.088	H-5, L+1 (28%); H-4, L+1 (−20%); H-3, L+2 (−21%); H-5, L+2 (27%); H-4, L+2 (22%); H-3, L+1 (−21%)
				576	0.060	H-3, L (44%); H, L (23%); H-5, L+2 (27%); H-4, L+2 (22%); H-3, L+1 (−21%)

[a] TD-DFT calculations were carried out at the CAM-B3LYP/6-31G(d) level of theory.

small differences in the absorption profile at the red side of the MLCT band. The $\pi \rightarrow \pi^*$ transition is further red-shifted to 448 nm and broadened into a single peak, and the MLCT band appears at 591 nm, with an increase in intensity. The asymmetry of the low-energy band remains, again implying further lower-energy transitions. The absorption profile of the trinuclear complex shows some significant differences from the previous cases and is not just an example of further red shifting of the bands. While the $\pi \rightarrow \pi^*$ transition shows a larger shift to 464 nm, the MLCT transition no longer appears as a single peak but as an absorption feature that extends from beyond 500 nm out to 700 nm. The red shift in both the $\pi \rightarrow \pi^*$ and MLCT transitions implies that the electronic structure of the component parts HATN-Me$_6$ and rhenium is being significantly perturbed.

DFT has been widely used in the study of metal polypyridyl complexes because of its utility and relative accuracy in providing insight into the electronic properties of such systems.[42−44] One method to check the efficacy of the calculations is to predict the vibrational spectra and compare them to the experimental data.[45−48] The validity of the DFT calculations may be tested by calculating the vibrational spectra (IR and Raman) and comparing these predicted spectra with experimental data.[39,49−53] The level of correlation was then quantified by using the mean absolute deviation (MAD) between the frequencies of the most intense peaks.[45,54−56] The experimental and calculated Raman spectra for the complexes are shown in Figure S2 in the Supporting Information. For the mono-, bi-, and trinuclear complexes studied herein, these are 8.8, 10.4, and 5.7 cm^{-1}, respectively, and this is considered a good correlation.

Previous studies have shown that hybrid functionals such as B3LYP do rather poorly in modeling charge-transfer systems such as those in the present study. The poor performance of these functionals for charge-transfer systems has been shown to be a combination of self-interaction error and the inability of B3LYP to account for long-range exchange.[57] This has led to the development of new functionals that overcome these problems, such as the popular CAM-B3LYP.[58,59] Such issues related to DFT have been recently reviewed by Vlček et al.[60] In order to better understand the performance of CAM-B3LYP in rhenium polypyridyl systems, a comparative study was undertaken using the B3LYP and CAM-B3LYP functionals. Initial calculations using the B3LYP functional showed very poor correlation with experiment. An attempt to improve this correlation by including solvation fields was also undertaken, but this also proved unsuccessful. For this reason, these calculations were not further pursued.

The results from the CAM-B3LYP calculations, which display a better simulation of the experimental data, are shown in Table 1. Results from the B3LYP calculation and calculated molecular orbital diagrams are shown in Tables S2 and S3 in the Supporting Information, respectively. In general, the B3LYP and CAM-B3LYP calculations display identical results with regard to the nature of the calculated transitions (i.e., the orbital contributions). However, the calculated energy of the transitions differs greatly depending on the choice of functional. The $\pi \rightarrow \pi^*$ transition energies were modeled well with the B3LYP functional, but the MLCT transitions were underestimated in energy. The CAM-B3LYP functional resulted in calculated MLCT

dx.doi.org/10.1021/ic200136t |*Inorg. Chem.* 2011, 50, 6093–6106

Table 2. Calculated Frontier Molecular Orbitals of the $(Re(CO)_3Cl)(HATN\text{-}Me_6)$, *syn*-$\{(Re(CO)_3Cl)_2(\mu\text{-}HATN\text{-}Me_6)\}$, and *syn*-$\{(Re(CO)_3Cl)_3(\mu\text{-}HATN\text{-}Me_6)\}$ Complexes[a]

	$(Re(CO)_3Cl)(HATN\text{-}Me_6)$	*syn*-$\{(Re(CO)_3Cl)_2(\mu\text{-}HATN\text{-}Me_6)\}$	*syn*-$\{(Re(CO)_3Cl)_3(\mu\text{-}HATN\text{-}Me_6)\}$
LUMO	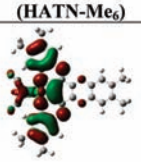	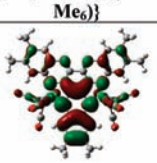	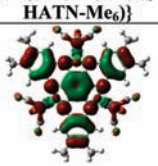
HOMO	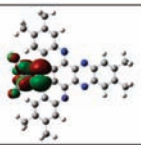	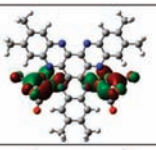	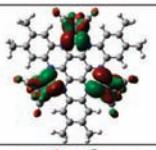
HOMO -1	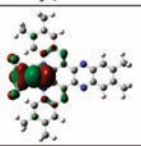	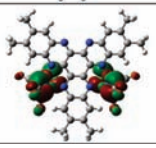	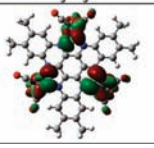

[a] The LUMOs of the anti complexes appear to be very similar to those of the syn complexes shown.

transition energies that were in close agreement with experimental data, yet the $\pi \rightarrow \pi^*$ transitions were overestimated in energy. This shows that B3LYP is an adequate method for determining the *nature* of electronic transitions in complicated polypyridyl complexes, but great care must be taken in interpreting the transition energies of such calculations.

The TD-DFT results for $(Re(CO)_3Cl)(HATN\text{-}Me_6)$ predict a single $\pi \rightarrow \pi^*$ transition at 363 nm, with a pair of MLCT transitions at 474 and 524 nm. The 524 nm transition is extremely weak ($f = 0.001$) and can be assigned as a low-intensity shoulder observed as the asymmetry of the MLCT band at ~600 nm in the electronic absorption spectrum. The MLCT transitions all terminate on the lowest unoccupied molecular orbital (LUMO), but the excitation from highest occupied molecular orbital (HOMO) → LUMO (524 nm) is much weaker than HOMO−1 → LUMO (474 nm). This is a consequence of the lower orbital overlap between the donor (HOMO dπ) and acceptor (LUMO π_L^*) orbitals than HOMO−1 (dπ) and LUMO (Table 2), which is responsible for the stronger transition. A similar phenomenon has been observed in computational studies on $Mn(CO)_3I(bipy)$; in these studies, the mixing of the halogen p orbitals with the manganese dπ molecular orbital could be used to rationalize the observed transition intensities.[61] The interpretation of DFT calculations with respect to the close interplay between the ligand-centered (LC) and MLCT states has been reviewed for ruthenium(II) and rhenium(I) complexes.[62] The calculated electronic structure of the binuclear complex shows no discernible differences between the syn and anti isomers. The calculated results for the binuclear complex are similar to those of the mononuclear complex, with a calculated red shift in the MLCT bands to 539 and 606 nm. The lower-energy transitions show some increase in intensity, but the MLCT is still dominated by the 539 nm band. The LUMO is also much more delocalized in the binuclear complex compared to the mononuclear species, but it is still not spread over the entire ligand. The red shift in the MLCT transition can be attributed to a lowering in the LUMO energy level because it is delocalized across the ligand. The electronic structure of the trinuclear species is significantly different from the previous two cases. Here delocalization of the LUMO is complete, and LUMO+1 and LUMO+2 have also decreased in energy and now contribute to the visible transitions. The calculated $\pi \rightarrow \pi^*$ transition is not particularly well modeled, but it does show (with both the B3LYP and CAM-B3LYP functionals) that LUMO, LUMO+1, and LUMO+2 are all involved in this transition. For the MLCT transitions, the situation is much more complicated. The transition involves orbitals ranging from HOMO−20 to HOMO, and this, coupled with the fact that LUMO+1 and LUMO+2 are also able to be accessed with visible light, means that there are now numerous combinations of excitations that can be achieved. The calculated MLCT transitions in Table 1 are only those with the strongest intensities; numerous weak transitions are calculated from 457 to 670 nm. The appearance of numerous transitions is consistent with the very broad MLCT transition observed in the electronic absorption spectrum.

Table 3. Reduction Potentials for Compounds in This Study

	$E_{red(1)}$/V vs SCE[a]	$E_{red(2)}$/V vs SCE
$HATN\text{-}Me_6$	−1.09	−1.40
$(Re(CO)_3Cl)(HATN\text{-}Me_6)$	−0.72	−0.45
anti-$\{(Re(CO)_3Cl)_2(\mu\text{-}HATN\text{-}Me_6)\}$	−0.05	−0.58
syn-$\{(Re(CO)_3Cl)_2(\mu\text{-}HATN\text{-}Me_6)\}$	−0.05	−0.63
anti-$\{(Re(CO)_3Cl)_3(\mu\text{-}HATN\text{-}Me_6)\}$	0.21	−0.16
syn-$\{(Re(CO)_3Cl)_3(\mu\text{-}HATN\text{-}Me_6)\}$	0.22	−0.16

[a] Reduction potentials are recorded relative to $DMFc^+$/DMFc and converted to SCE. The solvent was CH_2Cl_2 and the supporting electrolyte $TBAPF_6$. Irreversible oxidations were observed toward the solvent limit.

2.4. Electrochemistry. The reduction potentials for the $HATN\text{-}Me_6$ ligand and the $\{(Re(CO)_3Cl)_x(\mu\text{-}HATN\text{-}Me_6)\}$ complexes are shown in Table 3. Irreversible oxidations were observed close to the solvent limit. The reversible first and second reduction potentials are assigned as ligand-based reductions. The reduction potential for $HATN\text{-}Me_6$ is stabilized by almost 600 mV upon chelation of a single $\{Re(CO)_3Cl\}$ moiety. The binding of a second and third metal center has a diminishing

dx.doi.org/10.1021/ic200136t |*Inorg. Chem.* 2011, 50, 6093–6106

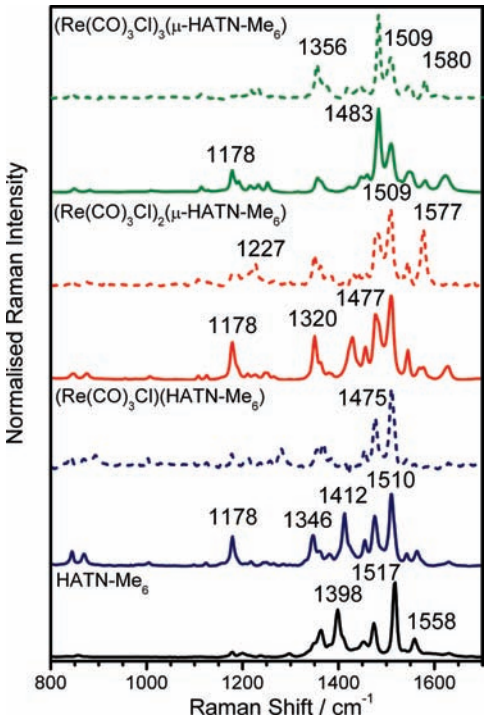

Figure 4. RR spectra of the HATN-Me_6 ligand and rhenium complexes thereof. Solid lines depict spectra obtained with an excitation line in resonance with the $\pi \rightarrow \pi^*$ transition (444 nm), while the dashed lines are spectra within the MLCT resonance (568.1 or 647 nm). The solution concentration was approximately 10^{-3} mol L^{-1} in CH_2Cl_2.

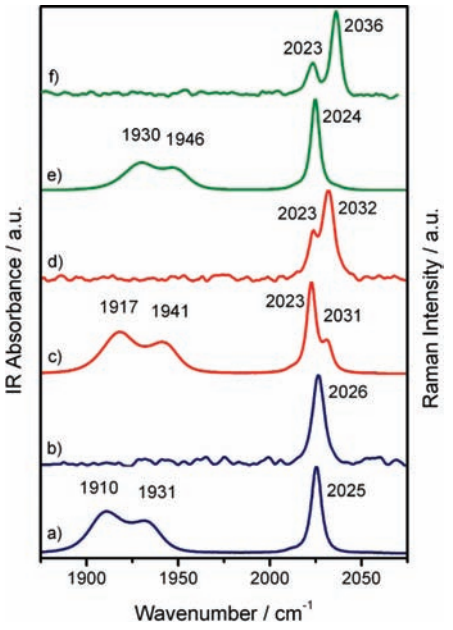

Figure 5. Traces a, c, and e showing FT-IR spectra and traces b, d, and f showing RR spectra of $(Re(CO)_3Cl)(HATN\text{-}Me_6)$, *syn*-$\{(Re(CO)_3Cl)_2(\mu\text{-}HATN\text{-}Me_6)\}$, and *syn*-$\{(Re(CO)_3Cl)_3(\mu\text{-}HATN\text{-}Me_6)\}$, respectively. All spectra were acquired in CH_2Cl_2. The RR spectrum of the mononuclear compound was acquired with an excitation wavelength of 568.1 nm, while 647 nm was used for the others.

effect, with the reduction potentials stabilized by 400 and 270 mV, respectively. These data are consistent with recent electrochemical studies on *syn*-$\{(Re(CO)_3Cl)_2(\mu\text{-}HATN\text{-}Me_6)\}$.[32]

The binuclear isomers show identical electrochemical behavior for their first reduction potentials but some differences for the second reduction potentials. The first and second reduction potentials for the isomers of the trinuclear complexes are virtually identical. This is consistent with the lowering in energy of the HATN based LUMOs as suggested by DFT calculations and observed in the UV−vis absorption spectra, where subsequent binding of $\{Re(CO)_3Cl\}$ moieties results in longer wavelengths of the MLCT absorption.

2.5. RR Spectroscopy. RR spectroscopy has been a widely used technique for investigating the photophysics of d^6 metal polypyridyl complexes.[17,54,63−66] In RR spectroscopy, the enhancement of signal intensities is determined by how well the vibrational modes mimic the structural distortions upon photoexcitation to the resonant electronic excited state.[67−69]

The RR spectra of the ligand and complexes are shown in Figure 4, while the calculated vibrational modes are shown in Figure S3 in the Supporting Information. The RR spectra of the complexes with $\pi \rightarrow \pi^*$ excitation show the same characteristic bands as the free ligand, except for a discernible peak at 1178 cm^{-1} in all complexes. There is very little shift in the energies of the vibrations between the mono-, bi-, and trinuclear complexes. The only band that shows any appreciable shift is the one at 1475 cm^{-1} in the mononuclear complex, which shifts to 1477 and 1483 cm^{-1} for the bi- and trinuclear species, respectively. The normal mode for this transition is associated with significant bond vibration about the chelating nitrogen atoms; the addition of rhenium centers to these sites, therefore, results in a change of the bond order and thus the energy required for vibration. The increased enhancement of the modes associated with the chelating nitrogen atoms is consistent with MLCT excitation.

Excitation resonant with the MLCT transition displays a rather different enhancement pattern across the family of complexes. The mononuclear complex displays only a small number of major bands at 1510 and 1476 cm^{-1}. These arise from an asymmetric ligand breathing mode localized on the aromatic rings closest to the point of ligation. The addition of the second rhenium unit gives rise to more Raman bands, with the major additional ones at 1577, 1320, and 1227 cm^{-1}. A similar enhancement pattern exists for $\{(Re(CO)_3Cl)_3(\mu\text{-}HATN\text{-}Me_6)\}$. These bands are associated with vibrations that are more delocalized compared to those of $(Re(CO)_3Cl)(HATN\text{-}Me_6)$. This arises from the fact that the excited-state molecular orbitals for the transitions are largely delocalized across the ligand, as discussed in section 2.3.

2.6. Ground-State Vibrational Spectroscopy. The ground-state FT-IR absorption and RR spectra in the carbonyl region of the complexes, acquired in CH_2Cl_2, are shown in Figure 5. The FT-IR spectrum of $(Re(CO)_3Cl)(HATN\text{-}Me_6)$ shows three carbonyl bands due to the facial arrangement of the $\{Re(CO)_3Cl\}$ unit with C_s symmetry, corresponding to three modes, as is illustrated in Figure 6. From lowest to highest energy, the vibrations are as follows: a′(2), out-of-phase stretch, a″, in-plane antisymmetric stretch; a′(1), in-phase symmetric stretch.[70] The syn and anti isomers of both the bi- and trinuclear complexes show only subtle differences in the carbonyl band frequencies between isomers.

Both the IR and Raman spectra of the binuclear complexes show splitting of the high-energy symmetric stretching band, which has been seen in previous examples of bimetallic $\{Re(CO)_3Cl\}$ units bound to a bridging ligand.[71] This can be

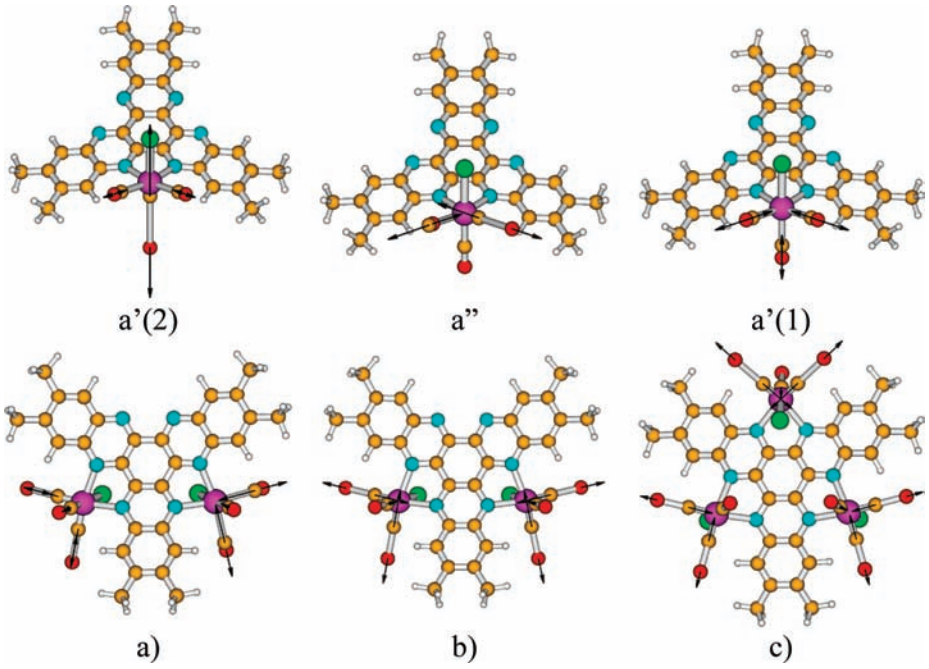

Figure 6. Eigenvector diagrams showing the CO vibrational bands for $(Re(CO)_3Cl)(HATN\text{-}Me_6)$ and (a) the out-of-phase a′(2) stretch of *syn*-$\{Re(CO)_3Cl)_2(\mu\text{-}HATN\text{-}Me_6)\}$, (b) the in-phase a″ stretch of *syn*-$\{(Re(CO)_3Cl)_2(\mu\text{-}HATN\text{-}Me_6)\}$, and (c) the in-phase a′(1) stretch of *anti*-$\{(Re(CO)_3Cl)_3(\mu\text{-}HATN\text{-}Me_6)\}$.

explained by coupling between the two metal centers: the individual a′(1) modes couple in-phase (Figure 6b) to give a band at 2031 cm^{-1} in both isomers and out-of-phase (Figure 6a) to give a band at 2023 cm^{-1}. For the trinuclear complexes, the coupling of the a′(1) modes results in the observation of two bands (2023 and 2036 cm^{-1}) in the Raman spectrum (Figure 5) split by 13 cm^{-1}, indicating stronger coupling than that in the binuclear complexes. Only one of the bands (2024 cm^{-1}) is observed in the IR spectrum. DFT calculations on these systems are in agreement with these observations. For the binuclear complex, two coupled a′(1) modes are predicted: they are separated by 7 cm^{-1}, with the higher frequency band being in-phase. The predicted IR band intensity (out-of-phase to in-phase) is 4:1, similar to that observed experimentally (Figure 5c); furthermore, the ratio of the Raman band intensities (out-of-phase to in-phase) is 1:5, in qualitative agreement with experiment (Figure 5d). For the trinuclear complex, a single in-phase mode (Figure 6c) is predicted with virtually no IR intensity, 11 cm^{-1} higher in frequency than the two degenerate out-of-phase modes predicted with strong IR intensity. In the experimental data, only the lower frequency band is observed. In contrast, the ratio of Raman intensities (out-of-phase to in-phase) is 1:3, similar to what is experimentally observed (Figure 5f).[72]

A subtle trend is present for the a′(2) and a″ vibrational frequencies with increasing number of $\{Re(CO)_3Cl\}$ centers, namely, an increase in the frequencies of these bands, i.e., ν_{CO} $Re_3 > \nu_{CO}$ $Re_2 > \nu_{CO}$ Re_1. This can be explained by the electron-withdrawing nature of the $\{Re(CO)_3Cl\}$ fragments. Lowering the electron density on the HATN ligand core results in a decrease in the available π-electron density for back-donation to the carbonyl π^* orbitals, which leads to an increase in the observed ν_{CO} frequencies.

2.7. TRIR Spectroscopy. Photoexcitation of $(Re(CO)_3Cl)$-$(HATN\text{-}Me_6)$ in CH_2Cl_2 with a 400 nm 150 fs laser pulse results in depletion of the ground-state bands within the instrument response time (0.6 ps; Figure 7). New absorption features are observed at higher energy in relation to the parent bands, which blue-shift and sharpen within 50 ps to give bands at 2058, 1998, and 1963 cm^{-1} (Table 4). These bands subsequently decay to reform the parent with a lifetime of 1.3 (±0.1) ns (Figure 8). These bands are assigned as a′(1), a′(2), and a″, respectively, by comparison with the two-dimensional IR results obtained for the

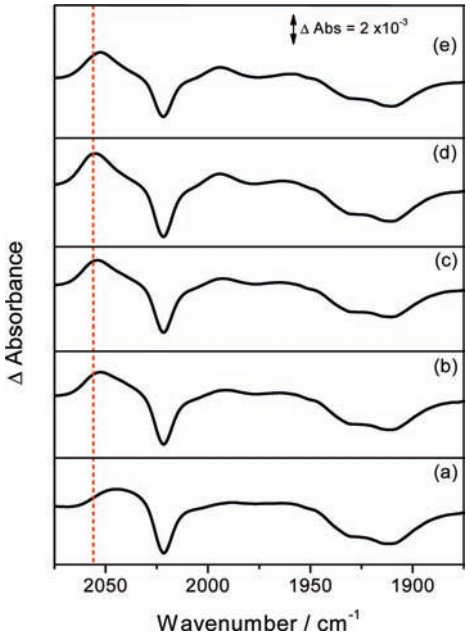

Figure 7. ps-TRIR spectra of $(Re(CO)_3Cl)(HATN\text{-}Me_6)$ at (a) 1, (b) 3, (c) 6, (d) 35, and (e) 350 ps after excitation. Spectra were acquired in CH_2Cl_2.

dx.doi.org/10.1021/ic200136t |*Inorg. Chem.* 2011, 50, 6093–6106

Table 4. IR ν_{CO} Bands in the Ground and Excited States

complex	ground state ν_{CO}/cm^{-1}	excited state ν_{CO}/cm^{-1}
$\{Re(CO)_3Cl(HATN\text{-}Me_6)\}$	2025, 1931,1910	2058, 1998, 1963
anti-$\{(Re(CO)_3Cl)_2(\mu\text{-}HATN\text{-}Me_6)\}$	2031 (sh), 2023, 1939, 1921	2062, 2012, 1902
syn-$\{(Re(CO)_3Cl)_2(\mu\text{-}HATN\text{-}Me_6)\}$	2031 (sh), 2023, 1941, 1917	2064, 2010, 1898
anti-$\{Re(CO)_3Cl)_3(\mu\text{-}HATN\text{-}Me_6)\}$	2024, 1947, 1930	2073, 2014, 1908
syn-$\{(Re(CO)_3Cl)_3(\mu\text{-}HATN\text{-}Me_6)\}$	2024, 1946, 1930	2073, 2014, 1908

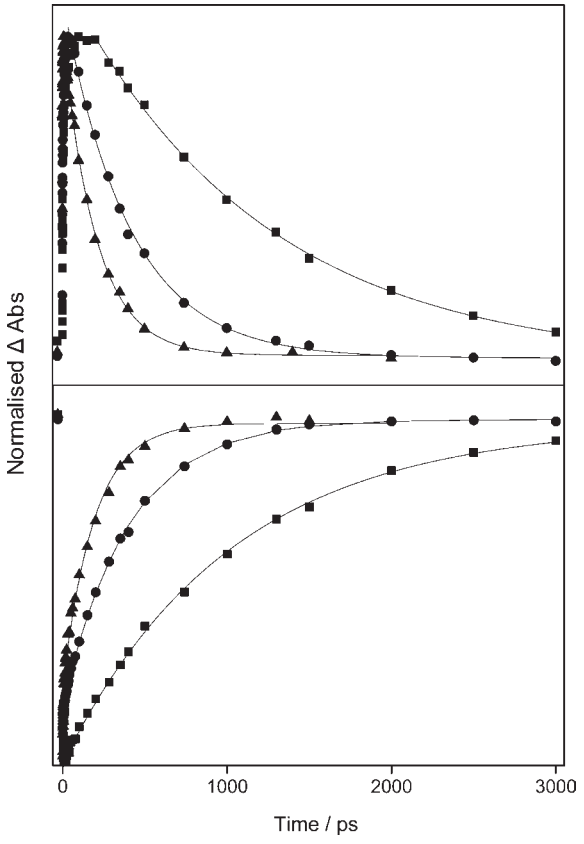

Figure 8. TRIR traces showing (upper) decay of excited-state bands and (lower) parent recovery of (a) $(Re(CO)_3Cl)(HATN\text{-}Me_6)$ (■), (b) *anti*-$(Re(CO)_3Cl)_2(\mu\text{-}HATN\text{-}Me_6)$ (●), and (c) *syn*-$(Re(CO)_3Cl)_3(\mu\text{-}HATN\text{-}Me_6)$ (▲) following 400 nm excitation.

^{3}MLCT state of $Re(bpy)(CO)_3Cl$.[73] The observed spectral changes are consistent with the population of a vibrationally hot state, which undergoes cooling over a ~50 ps time scale, followed by relaxation of the thermally equilibrated excited state (THEXI) over the longer time scale. The observation of a shift to higher wavenumber for the carbonyl ligand stretching modes is indicative of depopulation of the electron density at the rhenium metal, consistent with oxidation and the formation of an MLCT excited state.[43,73−80]

TRIR measurements were conducted on both the syn and anti isomers of $\{(Re(CO)_3Cl)_2(\mu\text{-}HATN\text{-}Me_6)\}$. The two isomers behaved indistinguishably from one another; spectra for the syn isomer are shown in Figure S4 in the Supporting Information. As observed previously, bleaching of the ground-state bands was observed for the shortest time delay. After ~50 ps, vibrational cooling is considered to have finished and the bands associated

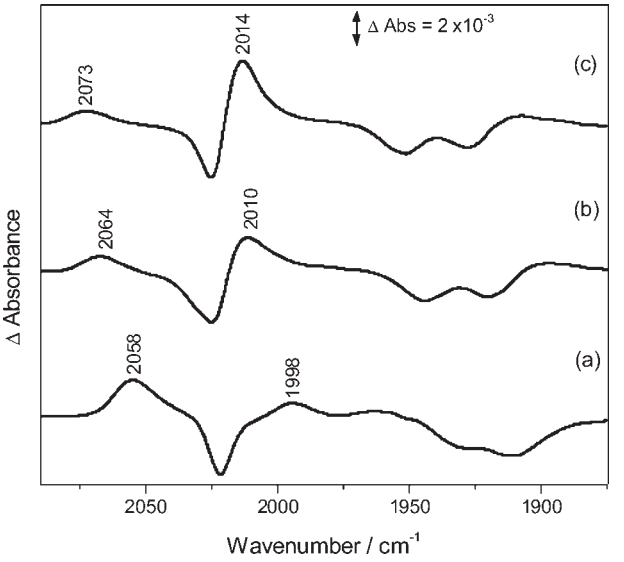

Figure 9. ps-TRIR spectra of (a) $(Re(CO)_3Cl)(HATN\text{-}Me_6)$, (b) *syn*-$\{(Re(CO)_3Cl)_2\ (\mu\text{-}HATN\text{-}Me_6)\}$ and (c) *syn*-$\{(Re(CO)_3Cl)_3\text{-}(\mu\text{-}HATN\text{-}Me_6)\}$ acquired 50 ps following 400 nm excitation.

with the THEXI state may be clearly observed (Figure 9). For the syn isomer, these features decay with a lifetime of 510 (±10) ps (Figure 8). In this case, two sets of bands are evident, namely, bands shifted to lower wavenumber relative to the parent (2010 and 1892 cm^{-1}) along with a band at higher energy (2064 cm^{-1}). This spectrum is consistent with a charge-transfer excitation in which oxidation is localized on one of the rhenium centers on the IR time scale; the shifts to lower wavenumber occur because the ligand radical anion back-bonds through the rhenium dπ orbitals to increase the electron density in the π^*_{CO} orbitals, and this thereby lowers the CO stretching frequencies.[71,81,82] Similar shifts have been observed in IR spectroelectrochemical reduction studies on *syn*-$\{(Re(CO)_3Cl)_2(\mu\text{-}HATN\text{-}Me_6)\}$.[32,83]

A similar spectrum is observed for *syn*-$\{(Re(CO)_3Cl)_3(\mu\text{-}HATN\text{-}Me_6)\}$ (Figure 9), and this allows comparison between the bi- and trinuclear complexes. The ν_{CO} band corresponding to the oxidized rhenium center lies at 2073 cm^{-1}, at higher energy relative to the binuclear, indicating increased oxidation of the absorbing $\{Re(CO)_3Cl\}$ unit with an increasing number of metal centers. This pattern of shifts on going from mono- to trinuclear complexes is consistent with the electron-withdrawing properties of the $\{Re(CO)_3Cl\}$ moieties. There is less back-donation from the reduced ligand to the oxidized rhenium in the MLCT excited state. Thus, the extent of oxidation in the MLCT excited state is greater for the trinuclear complex than for the bi- and mononuclear complexes. Additionally, a shift of the ν_{CO} band assigned

to the unoxidized rhenium center of *syn*-{$(Re(CO)_3Cl)_2(\mu$-HATN-$Me_6)$} from 2010 to 2014 cm^{-1} is observed on going from the bi- to trinuclear compound. The intensities of these features increase with increasing number of metal centers, corresponding to an increase in the number of unoxidized $\{Re(CO)_3Cl\}$ residues. Conversely, a decrease is observed for the relative intensity of the high-energy band. In summary, the bands that are blue-shifted from the ground-state feature at 2023−2025 cm^{-1} and appear at 2058 (mononuclear), 2064 (binuclear), and 2073 (trinuclear) cm^{-1} are attributed to the formal Re^{II} center in the MLCT state. Additionally, TRIR features red-shifted relative to the same ground-state bands at 2010 (binuclear) and 2014 (trinuclear) cm^{-1} are attributed to the spectator Re^{I} sites bound to more anionic ligands.

Molecular orbital pictures can also give insight into excited-state structures, as evidenced by a comparison of LUMO acceptor orbitals (Table 2). The transition of the mononuclear compound terminates on an orbital that is spatially close to the metal center, while the acceptor orbitals of the bi- and trinuclear compounds are more delocalized across the remainder of the HATN ligand. This is consistent with the picosecond (ps)-TRIR results, which show that the carbonyl bands associated with the oxidized metal center shift to higher wavenumber on going from mono- to bi- to trinuclear complexes. This is consistent with the nature of the acceptor molecular orbital; in the mononuclear complex, back-bonding between π^*_L through dπ to π^*_{CO} results in a lower wavenumber upshift for the CO stretches, but in the bi- and trinuclear complexes, the dispersed nature of π^*_L means that back-bonding to the oxidized metal is reduced, and thus the wavenumber upshift for the CO bound to the oxidized rhenium is greater.

The electron-withdrawing properties of the unoxidized Re^{I} centers that lead to the shifts of the Re^{I} and Re^{II} bands discussed above also reduce the lifetime of the excited state. The trinuclear complexes decay with a lifetime of ∼220 ps {syn, 215 (±15) ps; anti, 222 (±11) ps}; this is faster than the mono- and binuclear complexes, which show decay times of 1.3 (±0.1) ns and ∼400−500 ps {syn, 510 ± 10 ps; anti, 410 ± 20 ps}, respectively. This is consistent with the energy-gap law, which predicts an increase in the nonradiative decay with a decreasing energy gap between the ground and excited states.[84,85] Both the reduction potentials and MLCT absorption energies (see sections 2.4 and 2.3) are consistent with this. While vibrational cooling has been observed for the Re_2 and Re_3 complexes (Figures S4 and S5 in the Supporting Information), kinetic data could not be fitted because of overlap with the short decay times of the triplet excited state.

CONCLUSIONS

The syn and anti isomers of the binuclear {$(Re(CO)_3Cl)_2(\mu$-HATN-$Me_6)$} and trinuclear {$(Re(CO)_3Cl)_3(\mu$-HATN-$Me_6)$} complexes have been synthesized and separated. The assignment of isomers was achieved by X-ray crystallography. The binding of two and three $\{Re(CO)_3Cl\}$ moieties results in severe bending of the aromatic HATN-Me_6 unit in the crystal structures of the compounds. Intense $\pi \rightarrow \pi^*$ and MLCT absorptions in the visible region dominate the electronic spectra of the compounds. The trinuclear species have unique MLCT absorptions relative to the mono- and binuclear species, with the MLCT no longer appearing as a single peak but as a large region of absorption that extends from beyond 500 to 700 nm. The compounds are modeled with DFT, and the effectiveness of the calculations is checked by comparing the observed and simulated Raman spectra, which show a good correlation (MAD < 10 cm^{-1}) between experiment and theory. The UV−vis spectra are also simulated using TD-DFT; in this case, the accuracy of the modeling is strongly dependent on the nature of the transition; for the LC $\pi \rightarrow \pi^*$ transitions, the energies are predicted well by B3LYP but the MLCT transition energies are underestimated. The use of CAM-B3LYP, a functional that accounts for longer range interactions, improves the estimation of the MLCT transitions, but this functional is less effective in modeling the $\pi \rightarrow \pi^*$ transitions. In both cases, the principal molecular orbitals that contribute to the transitions, whether their energies are well predicted or not, are similar irrespective of the functional used.

The transitions of the complexes are examined experimentally using RR and TRIR spectroscopies. The RR studies support the TD-DFT calculations in showing enhancement of bands consistent with MLCT excitation in the red and LC modes with blue excitation. TRIR spectroscopy of the compounds confirms that the lowest excited state is MLCT in nature; furthermore, the extent of charge transfer (metal-to-ligand character) is greatest for the trinuclear complexes and least for the mononuclear complexes.

EXPERIMENTAL SECTION

Materials. $Re(CO)_5Cl$, hexaketocylohexane, and 4,5-dimethyl-1, 2-phenylenediamine were used as received. HATN-Me_6 and $(Re(CO)_3Cl)$(HATN-Me_6) were synthesized according to literature procedures.[10]

syn/anti-{(Re(CO)$_3$Cl)$_2$(μ-HATN-Me$_6$)}. A total of 0.35 g of HATN-Me_6 (0.747 mmol) and 2 equiv of $Re(CO)_5Cl$ (0.54 g, 1.49 mmol) were refluxed in 170 mL of chloroform for 12 h under an N_2 atmosphere. The resulting dark-brown solution was evaporated to dryness under vacuum. The crude brown solid was dissolved in the minimum volume of CH_2Cl_2, and the two isomers were separated by column chromatography on silica gel (eluant, CH_2Cl_2/ethyl acetate 5%). First fraction R_f = 0.5 and second fraction 0.2. It was also common for a small amount of the trinuclear complex to be formed; this eluted with an R_f of 0.70.

anti-{(Re(CO)$_3$Cl)$_2$(μ-HATN-Me$_6$)}, Yield = 0.306 g (0.283 mmol), 38%. ^{1}H NMR (400 MHz): methyl protons, δ 2.74 (s, 3H), 2.81 (s, 3H), 2.83 (s, 3H); aromatic protons, δ 8.59 (s, 1H), 8.78 (s, 1H), 8.91, (s, 1H). Anal. Calcd for $C_{36}H_{24}N_6O_6Cl_2Re_2$; C, 40.04; H, 2.24; N, 7.78. Found: C, 40.32; H, 2.64; N, 7.40. ESI POS: *m/z* 1103.01 ({$(Re(CO)_3Cl)_2(\mu$-HATN-$Me_6)$} + Na^+), 1118.98 ({$(Re(CO)_3Cl)_2$ (μ-HATN-Me_6)} + K^+).

syn-{(Re(CO)$_3$Cl)$_2$(μ-HATN-Me$_6$)}, Yield = 0.322 g (0.299 mmol), 40%. Crystals suitable for X-ray diffraction were grown from the slow diffusion of hexane into a $CHCl_3$ solution. ^{1}H NMR (400 MHz): methyl protons, δ 2.74 (s, 3H), 2.80 (s, 3H), 2.83 (s, 3H); aromatic protons, δ 8.59 (s, 1H), 8.86 (s, 1H), 8.99 (s, 1H). Anal. Calcd for $C_{36}H_{24}N_6O_6Cl_2Re_2$; C, 40.04; H, 2.24; N, 7.78. Found: C, 39.90; H, 2.10; N, 7.53. ESI POS: *m/z* 1103.01 ({$(Re(CO)_3Cl)_2$ (μ-HATN-Me_6)} + Na^+), 1118.98 ({$(Re(CO)_3Cl)_2$ (μ-HATN-Me_6)} + K^+).

anti-{(Re(CO)$_3$Cl)$_3$(μ-HATN-Me$_6$)}. A total of 0.200 g of HATN-Me_6 (0.427 mmol) and 3 equiv of $Re(CO)_5Cl$ (0.463 g, 1.28 mmol) were refluxed in 150 mL of chloroform for 12 h under an N_2 atmosphere. The resulting dark-brown solution was evaporated under vacuum to dryness. The crude brown solid was dissolved in the minimum volume of CH_2Cl_2 and purified by column chromatography on silica gel (eluant, CH_2Cl_2/ethyl acetate 5%) to give *anti*-{$(Re(CO)_3Cl)_3(\mu$-HATN-$Me_6)$} with an R_f of 0.70. Yield = 0.514 g (0.371 mmol, 87%. Crystals suitable for X-ray diffraction were grown from the slow diffusion of hexane into a CH_2Cl_2

dx.doi.org/10.1021/ic200136t |*Inorg. Chem.* 2011, 50, 6093–6106

solution. ^{1}H NMR (400 MHz): methyl protons, δ 2.86 (s, 9H); aromatic protons, δ 8.86 (s, 1H), 8.91 (s, 1H), 8.93 (s, 1H). Anal. Calcd for $C_{39}H_{24}N_6O_9Cl_3Re_3$: C, 33.81; H, 1.75; N, 6.07. Found: C, 34.09; H, 1.91; N, 5.81. ESI POS: m/z 1408.19 ({(Re(CO)$_3$Cl)$_3$(μ-HATN-Me$_6$)} + Na$^+$).

syn-{*(Re(CO)$_3$Cl)$_3$(μ-HATN-Me$_6$)*}. A total of 0.041 g of *syn*-{(Re(CO)$_3$Cl)$_2$(μ-HATN-Me$_6$)} (3.79×10^{-5} mol) and 0.0014 g of Re(CO)$_5$Cl were refluxed in 25 mL of degassed toluene under an N_2 atmosphere for 6 h. The crude brown solid was dissolved in the minimum volume of CH_2Cl_2 and loaded onto a silica gel column (eluant, CH_2Cl_2/acetonitrile 4%). Yield = 0.043 g (3.11×10^{-5} mol, 82%). ^{1}H NMR (400 MHz): methyl protons, δ 2.85 (s, 3H); aromatic protons, δ 8.96 (s, 1H). Anal. Calcd for $C_{39}H_{24}N_6O_9Cl_3Re_3$: C, 33.81; H, 1.75; N, 6.07. Found: C, 34.02; H, 1.80; N, 6.31. ESI POS: m/z 1408.19 ({(Re(CO)$_3$Cl)$_3$(μ-HATN-Me$_6$)} + Na$^+$).

Physical Measurements. Aldrich spectroscopic grade or HP-grade solvents were used for all spectroscopic measurements. Spectral data were analyzed using *GRAMS/32 AI* (Galactic Industries) software. TRIR data were analyzed by custom in-house built software. Mass spectra were acquired using a Micromass LCT instrument for electrospray measurement or a Shimadzu QP8000 α with an electrospray ionization (ESI) probe. Microanalyses were carried out at the Campbell Microanalysis Laboratory at the University of Otago. ^{1}H NMR spectra of $CDCl_3$ solutions were recorded on a Varian 400 MHz spectrometer at room temperature. All spectra were referenced to the residual $CDCl_3$ peak at 7.26 ppm.

Absorption spectra were measured at room temperature on a Varian Cary 500 UV−vis/NIR spectrophotometer with Cary WinUV scan application software. A scan rate of 200 nm min^{-1} was employed between 200 and 900 nm. Sample concentrations were between 10^{-5} and 10^{-6} M in CH_2Cl_2. Crystal data, data collection, and refinement parameters are listed in Table S1 in the Supporting Information. Measurements were made with a Bruker diffractometer equipped with an Apex II charge-coupled device area detector using graphite-monochromated Mo Kα (λ = 0.710 73 Å) radiation. The structures were solved by direct methods and refined on F^2 by use of all data in full-matrix least-squares procedures, with all non-hydrogen atoms refined anisotropically.

The electrochemical cell for cyclic voltammetry comprises a 1-mm-diameter platinum rod working electrode embedded in a KeL-F cylinder with a platinum auxiliary electrode and a Ag/AgCl reference electrode. The potential of the cell was controlled by an EG&G PAR 273 A potentiostat with model 270 software. Solution concentrations were typically about 10^{-3} M in CH_2Cl_2 with 0.1 M tetrabutylammonium hexafluorophosphate ($TBAPF_6$) added as a supporting electrolyte. Solutions were purged with N_2 for approximately 5 min prior to measurement. $TBAPF_6$ was recrystallized from ethyl acetate, dried under vacuum at 70 °C for 10 h, and then kept at 90 °C until use. The scanning speed used was 0.1 V s^{-1}. Cyclic voltammograms were calibrated against the decamethylferrocenium/decamethylferrocene (DMFc) couple (−0.012 V in CH_2Cl_2)[86] and are reported relative to the saturated calomel electrode (SCE) for comparison with other data by subtracting 0.045 V.[87]

FT-Raman spectra were collected on powder samples using a Bruker IFS-55 interferometer with a FRA/106 S attachment. The excitation source was a Nd:YAG laser with an excitation wavelength of 1064 nm. A liquid-nitrogen-cooled germanium diode (D418T) was used to detect Raman photons. All spectra were measured over 64−256 scans with a laser power of 80 mW at the sample and a spectral resolution of 4 cm^{-1}. FT-IR spectra were taken using a Perkin-Elmer 100 FT-IR spectrometer, on CH_2Cl_2 solutions of typically 10^{-3} M in concentration, using a resolution of 0.5 cm^{-1}

RR spectra were recorded for all compounds by using a setup described previously.[46,88,89] Excitation wavelengths of 444, 568.1, and 647 nm were employed, and concentrations of the solutions were typically 5−7 mM in CH_2Cl_2.

ps-TRIR Apparatus. The ps-TRIR apparatus is located at Nottingham University and is based upon the PIRATE facility at the Rutherford Appleton Laboratory[90] which has been described previously.[91] Briefly, the output from a commercial Ti:sapphire oscillator (MaiTai)/regenerative amplifier system (Spitfire Pro, Spectra Physics) is split and used to generate 400 nm pump pulses and a tunable mid-IR pulse with a spectral bandwidth of 180 cm^{-1} and a pulse energy of ca. 2 μJ at 2000 cm^{-1}. Half of the IR pulse is reflected onto a single-element mercury−cadmium telluride (MCT) detector (Kolmar Technology) to serve as a reference, and the other half serves as the probe beam, which is focused and overlaps with the pump beam at the sample position. The 400 nm pump pulse is optically delayed (up to 3 ns) by a translation stage (LMA Actuator, Aerotech) and focused onto the sample with a quartz lens. The polarization of the pump pulse is set at the magic angle (54.7°) relative to the probe pulse to recover the isotropic absorption spectrum. The broad-band-transmitted probe pulse is detected with an MCT array detector (Infrared Associates), which consists of 128 elements (1 mm high and 0.25 mm wide). The array detector is mounted in the focal plane of a 250 mm IR spectrograph (DK240, Spectra Product) with a 150 g mm^{-1} grating, resulting in a spectral resolution of ca. 4 cm^{-1} at 2000 cm^{-1}. The signals from the array detector elements and the single-element detector are amplified with a 144-channel amplifier and digitized by a 16-bit analogue-to-digital converter (IR-0144, Infrared Systems Development Corp.). A Harrick flowing solution cell with 2-mm-thick CaF_2 windows and a path length of 500 μm is mounted on a motorized cell mount that moves the cell rapidly in x and y dimensions throughout the experiment. Consequently, each laser pulse illuminates a different volume of the sample, reducing heating and degradation of the sample solution.

COMPUTATIONAL METHODS

In vacuo geometry optimizations and calculations of vibrational frequencies were performed using DFT, employing a B3LYP functional. In vacuo TD-DFT calculations were completed with the B3LYP and CAM-B3YLP[58] functionals for a comparison of the performance of each of these systems. All of the DFT calculations employed LANL2DZ effective core potential for modeling of the rhenium atoms, which has shown to be suitable in related systems.[39,46] The remaining atoms were modeled with the 6-31G(d) basis set. The *Gaussian09* suite of programs was used for all calculations.[92] Symmetry constraints were used where applicable. The calculated Raman intensities were calibrated for Raman activity with 1064 nm excitation.[54] Calculated vibrational energies (in wavenumbers) were scaled by 0.975, a factor that we have found to be suitable for metal polypyridyl complexes.[14,46,54,93] Visualizations of calculated molecular orbitals were done with *GaussViewW* (Gaussian Inc.),[92] and vibrational modes were illustrated with the *Molden* package.[94]

ASSOCIATED CONTENT

Supporting Information. X-ray crystallographic data and structure refinement data (Table S1), intermolecular $\pi-\pi$-stacking figure (Figure S1), calculated and experimental FT-Raman spectra of the rhenium complexes (Figure S2), calculated electronic transitions and molecular orbitals using the B3LYP functional (Tables S2 and S3), calculated modes of vibration (Figure S3), and ps-TRIR spectra of *syn*-{(Re(CO)$_3$Cl)$_2$-(μ-HATN-Me$_6$)} and *syn*-{(Re(CO)$_3$Cl)$_3$)(μ-HATN-Me$_6$)} (Figures S4 and S5). This material is available free of charge via the Internet at http://pubs.acs.org.

AUTHOR INFORMATION

Corresponding Author

*E-mail: mike.george@nottingham.ac.uk (M.W.G.), kgordon@chemistry.otago.ac.nz (K.C.G.).

ACKNOWLEDGMENT

We thank the EPSRC (Grant EP/G013330 to X.-Z.S., C.A.C., and M.W.G.), the University of Otago, the Royal Society of New Zealand (Marsden Fund UOO611), the MacDiarmid Institute for Advanced Materials and Nanotechnology, and the Foundation of Research Science and Technology for funding. M.W.G. gratefully acknowledges receipt of a Royal Society Wolfson Merit Award. We also thank Scott Cameron for assistance in X-ray crystallography collection and graphical presentation.

REFERENCES

(1) Ong, C. W.; Liao, S.-C.; Chang, T. H.; Hsu, H.-F. *Tetrahedron Lett.* **2003**, *44*, 1477–1480.

(2) Crispin, X.; Cornil, J.; Friedlein, R.; Okudaira, K. K.; Lemaur, V.; Crispin, A.; Kestemont, G.; Lehmann, M.; Fahlman, M.; Lazzaroni, R.; Geerts, Y.; Wendin, G.; Ueno, N.; Bredas, J.-L.; Salaneck, W. R. *J. Am. Chem. Soc.* **2004**, *126*, 11889–11899.

(3) Bock, H.; Babeau, A.; Seguy, I.; Jolinat, P.; Destruel, P. *ChemPhysChem* **2002**, *3*, 532–535.

(4) Kestemont, G.; Halleux, V. d.; Lehmann, M.; Ivanov, D. A.; Watson, M.; Geerts, Y. H. *Chem. Commun.* **2001**, 2074–2075.

(5) Kaafarani, B. R.; Kondo, T.; Yu, J.; Zhang, Q.; Dattilo, D.; Risko, C.; Jones, S. C.; Barlow, S.; Domercq, B.; Amy, F.; Kahn, A.; Bredas, J.-L.; Kippelen, B.; Marder, S. R. *J. Am. Chem. Soc.* **2005**, *127*, 16358–16359.

(6) Clark, J.; Archer, R.; Redding, T.; Foden, C.; Tant, J.; Geerts, Y.; Friend, R. H.; Silva, C. *J. Appl. Phys.* **2008**, *103*, 124510-1–124510-6.

(7) Yip, H.-L.; Zhou, J.; Ma, H.; Tian, Y.; Tucker, N. M.; Jen, A. K. Y. *J. Am. Chem. Soc.* **2006**, *128*, 13042–13043.

(8) Kitagawa, S.; Masaoka, S. *Coord. Chem. Rev.* **2003**, *246*, 73–88.

(9) Elias, B.; Kirsch-De Mesmaeker, A. *Coord. Chem. Rev.* **2006**, *250*, 1627–1641.

(10) Catalano, V. J.; Larson, W. E.; Olmstead, M. M.; Gray, H. B. *Inorg. Chem.* **1994**, *33*, 4502–4509.

(11) Budd, P. M.; Ghanem, B.; Msayib, K.; McKeown, N. B.; Tattershall, C. *J. Mater. Chem.* **2003**, *13*, 2721–2726.

(12) Patra, S.; Sarkar, B.; Ghumaan, S.; Fiedler, J.; Kaim, W.; Lahiri, G. K. *Dalton Trans.* **2004**, 754–758.

(13) Ghumaan, S.; Sarkar, B.; Patil, M. P.; Fiedler, J.; Sunoj, R. B.; Kaim, W.; Lahiri, G. K. *Polyhedron* **2007**, *26*, 3409–3418.

(14) Lind, S. J.; Walsh, T. J.; Blackman, A. G.; Polson, M. I. J.; Irwin, G. I. S.; Gordon, K. C. *J. Phys. Chem. A* **2009**, *113*, 3566–3575.

(15) Roy, S.; Sarkar, B.; Duboc, C.; Fiedler, J.; Sarper, O.; Lissner, F.; Mobin, S. M.; Lahiri, G. K.; Kaim, W. *Chem.—Eur. J.* **2009**, *15*, 6932–6939.

(16) Coleman, A.; Brennan, C.; Vos, J. G.; Pryce, M. T. *Coord. Chem. Rev.* **2008**, *252*, 2585–2595.

(17) Polo, A. S.; Itokazu, M. K.; Murakami Iha, N. Y. *Coord. Chem. Rev.* **2004**, *248*, 1343–1361.

(18) Takeda, H.; Koike, K.; Inoue, H.; Ishitani, O. *J. Am. Chem. Soc.* **2008**, *130*, 2023–2031.

(19) Takeda, H.; Ishitani, O. *Coord. Chem. Rev.* **2010**, *254*, 346–354.

(20) Yam, V. W.-W.; Lo, K. K.-W.; Cheung, K.-K.; Kong, R. Y.-C. *J. Chem. Soc., Chem. Commun.* **1995**, 1191–1193.

(21) Lo, K. K.-W.; Louie, M.-W.; Zhang, K. Y. *Coord. Chem. Rev.* **2010**, *254*, 2603–2622.

(22) Wu, J.; Li, H. Y.; Kang, L. C.; Li, D. P.; Li, H. R.; Zhou, X. H.; Sui, Y.; Zheng, Y. X.; Zuo, J. L.; You, X. Z. *J. Photochem. Photobiol., A* **2010**, *211*, 135–142.

(23) Li, X.; Zhang, D. Y.; Li, W. L.; Chu, B.; Han, L. L.; Li, T. L.; Su, Z. S.; Zhu, J. Z.; Wu, S. H.; Chen, Y. R.; Lei, P.; Hu, Z. Z.; Zhang, Z. *Synth. Met.* **2009**, *159*, 1340–1344.

(24) Fu, C.; Li, M.; Su, Z.; Hong, Z.; Li, W.; Li, B. *Appl. Phys. Lett.* **2006**, *88*, 093507.

(25) David, G.; Walsh, P. J.; Gordon, K. C. *Chem. Phys. Lett.* **2004**, *383*, 292–296.

(26) Lundin, N. J.; Blackman, A. G.; Gordon, K. C.; Officer, D. L. *Angew. Chem., Int. Ed.* **2006**, *45*, 2582–2584.

(27) Mizoguchi, S. K.; Patrocinio, A. O. T.; Ilha, N. Y. M. *Synth. Met.* **2009**, *159*, 2315–2317.

(28) Si, Z. J.; Li, J.; Li, B.; Zhao, F. F.; Liu, S. Y.; Li, W. L. *Inorg. Chem.* **2007**, *46*, 6155–6163.

(29) Walsh, P. J.; Lundin, N. J.; Gordon, K. C.; Kim, J. Y.; Lee, C. H. *Opt. Mater.* **2009**, *31*, 1525–1531.

(30) Yamamoto, Y.; Sawa, S.; Funada, Y.; Morimoto, T.; Falkenström, M.; Miyasaka, H.; Shishido, S.; Ozeki, T.; Koike, K.; Ishitani, O. *J. Am. Chem. Soc.* **2008**, *130*, 14659–14674.

(31) Benkstein, K. D.; Hupp, J. T.; Stern, C. L. *Angew. Chem., Int. Ed.* **2000**, *39*, 2891–2893.

(32) Roy, S.; Kubiak, C. P. *Dalton Trans.* **2010**, *39*, 10937–10943.

(33) Alfonso, M.; Stoeckli-Evans, H. *Acta Crystallogr., Sect. E: Struct. Rep. Online* **2001**, *E57*, o242–o244.

(34) Janiak, C. *J. Chem. Soc., Dalton Trans.* **2000**, 3885–3896.

(35) Piglosiewicz, I. M.; Beckhaus, R.; Saak, W.; Haase, D. *J. Am. Chem. Soc.* **2005**, *127*, 14190–14191.

(36) Bu, X.-H.; Tanaka, K.; Shionoya, M.; Biradha, K.; Yamaguchi, T.; Nishimura, M.; Ito, T. *Chem. Commun.* **2000**, 1953–1954.

(37) Yam, V. W.-W.; Lau, V. C.-Y.; Cheung, K.-K. *Organometallics* **1995**, *14*, 2749–2753.

(38) Kirchhoff, J. R.; Kirschbaum, K. *Polyhedron* **1998**, *17*, 4033–4039.

(39) Lundin, N. J.; Walsh, P. J.; Howell, S. L.; Blackman, A. G.; Gordon, K. C. *Chem.—Eur. J.* **2008**, *14*, 11573–11583.

(40) Orsa, D. K.; Haynes, G. K.; Pramanik, S. K.; Iwunze, M. O.; Greco, G. E.; Ho, D. M.; Krause, J. A.; Hill, D. A.; Williams, R. J.; Mandal, S. K. *Inorg. Chem. Commun.* **2008**, *11*, 1054–1056.

(41) Polson, M. I. J.; Howell, S. L.; Flood, A. H.; Burrell, A. K.; Blackman, A. G.; Gordon, K. C. *Polyhedron* **2004**, *23*, 1427–1439.

(42) Dattelbaum, D. M.; Martin, R. L.; Schoonover, J. R.; Meyer, T. J. *J. Phys. Chem. A* **2004**, *108*, 3518–3526.

(43) Dattelbaum, D. M.; Omberg, K. M.; Hay, P. J.; Gebhart, N. L.; Martin, R. L.; Schoonover, J. R.; Meyer, T. J. *J. Phys. Chem. A* **2004**, *108*, 3527–3536.

(44) Walsh, P. J.; Gordon, K. C.; Lundin, N. J.; Blackman, A. G. *J. Phys. Chem. A* **2005**, *109*, 5933–5942.

(45) Fraser, M. G.; Blackman, A. G.; Irwin, G. I. S.; Easton, C. P.; Gordon, K. C. *Inorg. Chem.* **2010**, *49*, 5180–5189.

(46) Horvath, R.; Otter, C. A.; Gordon, K. C.; Brodie, A. M.; Ainscough, E. W. *Inorg. Chem.* **2010**, *49*, 4073–4083.

(47) Howell, S. L.; Gordon, K. C. *J. Raman Spectrosc.* **2008**, *39*, 813–826.

(48) Waterland, M. R.; Howell, S. L.; Gordon, K. C. *J. Phys. Chem. A* **2007**, *111*, 4604–4611.

(49) Clarke, T. M.; Gordon, K. C.; Officer, D. L.; Hall, S. B.; Collis, G. E.; Burrell, A. K. *J. Phys. Chem. A* **2003**, *107*, 11505–11516.

(50) Cleland, D. M.; Irwin, G.; Wagner, P.; Officer, D. L.; Gordon, K. C. *Chem.—Eur. J.* **2009**, *15*, 3682–3690.

(51) Earles, J. C.; Gordon, K. C.; Officer, D. L.; Wagner, P. *J. Phys. Chem. A* **2007**, *111*, 7171–7180.

(52) Howell, S. L.; Gordon, K. C. *J. Phys. Chem. A* **2006**, *110*, 4880–4887.

(53) Karnahl, M.; Tschierlei, S.; Kuhnt, C.; Dietzek, B.; Schmitt, M.; Popp, J.; Schwalbe, M.; Krieck, S.; Goerls, H.; Heinemann, F. W.; Rau, S. *Dalton Trans.* **2010**, *39*, 2359–2370.

(54) Horvath, R.; Gordon, K. C. *Coord. Chem. Rev.* **2010**, *254*, 2505–2518.

(55) Lundin, N. J.; Walsh, P. J.; Howell, S. L.; McGarvey, J. J.; Blackman, A. G.; Gordon, K. C. *Inorg. Chem.* **2005**, *44*, 3551–3560.

(56) Wagner, K.; Crowe, L. L.; Wagner, P.; Gambhir, S.; Partridge, A. C.; Earles, J. C.; Clarke, T. M.; Gordon, K. C.; Officer, D. L. *Macromolecules* **2010**, *43*, 3817–3827.

(57) Dreuw, A.; Head-Gordon, M. *J. Am. Chem. Soc.* **2004**, *126*, 4007–4016.
(58) Yanai, T.; Tew, D. P.; Handy, N. C. *Chem. Phys. Lett.* **2004**, *393*, 51–57.
(59) Guthmuller, J.; Gonzalez, L. *Phys. Chem. Chem. Phys.* **2010**, *12*, 14812–14821.
(60) Vlček, A., Jr.; Zális, S. *Coord. Chem. Rev.* **2007**, *251*, 258–287.
(61) Stor, G. J.; Stufkens, D. J.; Vernooijs, P.; Baerends, E. J.; Fraanje, J.; Goubitz, K. *Inorg. Chem.* **1995**, *34*, 1588–1594.
(62) Stufkens, D. J.; Vlcek, A. *Coord. Chem. Rev.* **1998**, *177*, 127–179.
(63) Herrmann, C.; Neugebauer, J.; Presselt, M.; Uhlemann, U.; Schmitt, M.; Rau, S.; Popp, J.; Reiher, M. *J. Phys. Chem. B* **2007**, *111*, 6078–6087.
(64) Bradley, P. G.; Kress, N.; Hornberger, B. A.; Dallinger, R. F.; Woodruff, W. H. *J. Am. Chem. Soc.* **1981**, *103*, 7441–7446.
(65) Caspar, J. V.; Westmoreland, T. D.; Allen, G. H.; Bradley, P. G.; Meyer, T. J.; Woodruff, W. H. *J. Am. Chem. Soc.* **1984**, *106*, 3492–3500.
(66) Dallinger, R. F.; Woodruff, W. H. *J. Am. Chem. Soc.* **1979**, *101*, 4391–4393.
(67) Hirakawa, A. Y.; Tsuboi, M. *Science* **1975**, *188*, 359–361.
(68) Clark, R. J. H.; Dines, T. J. *Angew. Chem.* **1986**, *98*, 131–160.
(69) Stufkens, D. J. *Comments Inorg. Chem.* **1992**, *13*, 359–385.
(70) Gamelin, D. R.; George, M. W.; Glyn, P.; Grevels, F.-W.; Johnson, F. P. A.; Klotzbuecher, W.; Morrison, S. L.; Russell, G.; Schaffner, K.; Turner, J. J. *Inorg. Chem.* **1994**, *33*, 3246–3250.
(71) Abbott, L. C.; Arnold, C. J.; Ye, T. Q.; Gordon, K. C.; Perutz, R. N.; Hester, R. E.; Moore, J. N. *J. Phys. Chem. A* **1998**, *102*, 1252–1260.
(72) Some care is required in comparing the calculated Raman intensities with experimental data because of the resonance effect; however, it is unlikely that these a′(1) would differ greatly in their resonance enhancement, and thus the calculated normal Raman intensities may be used qualitatively.
(73) Bredenbeck, J.; Helbing, J.; Hamm, P. *J. Am. Chem. Soc.* **2004**, *126*, 990–991.
(74) George, M. W.; Turner, J. J. *Coord. Chem. Rev.* **1998**, *177*, 201–217.
(75) Turner, J. J.; George, M. W.; Johnson, F. P. A.; Westwell, J. R. *Coord. Chem. Rev.* **1993**, *125*, 101–114.
(76) George, M. W.; Turner, J. J.; Westwell, J. R. *J. Chem. Soc., Dalton Trans.* **1994**, 2217–2219.
(77) George, M. W.; Johnson, F. P. A.; Turner, J. J.; Westwell, J. R. *J. Chem. Soc., Dalton Trans.* **1995**, 2711–2718.
(78) Easun, T. L.; Alsindi, W. Z.; Towrie, M.; Ronayne, K. L.; Sun, X.-Z.; Ward, M. D.; George, M. W. *Inorg. Chem.* **2008**, *47*, 5071–5078.
(79) Butler, J. M.; George, M. W.; Schoonover, J. R.; Dattelbaum, D. M.; Meyer, T. J. *Coord. Chem. Rev.* **2007**, *251*, 492–514.
(80) Easun, T. L.; Alsindi, W. Z.; Deppermann, N.; Towrie, M.; Ronayne, K. L.; Sun, X.-Z.; Ward, M. D.; George, M. W. *Inorg. Chem.* **2009**, *48*, 8759–8770.
(81) Kuimova, M. K.; Gordon, K. C.; Howell, S. L.; Matousek, P.; Parker, A. W.; Sun, X.-Z.; Towrie, M.; George, M. W. *Photochem. Photobiol. Sci.* **2006**, *5*, 82–87.
(82) An alternative interpretation for the pattern of band shifts is that we are probing an equilibrium of states that are MLCT and LC π,π^* in character. This interpretation is not favored because no such pattern is observed for the mononuclear complex, yet that complex has the LC and MLCT states closest in energy. Furthermore, in the bi- and trinuclear complexes, the MLCT states are significantly stabilized relative to the LC states, as evidenced by the UV−vis and electrochemical data. Additional evidence is provided by the excited-state lifetime, with bi- and trinuclear complexes having significantly shorter lifetimes than the monosubstituted compound. For a given compound, LC $^3\pi-\pi$ excited states generally have longer lifetimes than ^{3}MLCT excited states, and the faster excited-state decay of the bi- and trinuclear complexes suggests that the additional ν_{CO} bands seen in the excited-state IR spectrum are not due to the equilibrium of states that are MLCT and LC $\pi-\pi^*$ in character.
(83) Herrera, J.-M.; Pope, S. J. A.; Meijer, A. J. H. M.; Easun, T. L.; Adams, H.; Alsindi, W. Z.; Sun, X.-Z.; George, M. W.; Faulkner, S.; Ward, M. D. *J. Am. Chem. Soc.* **2007**, *129*, 11491–11504.
(84) Caspar, J. V.; Kober, E. M.; Sullivan, B. P.; Meyer, T. J. *J. Am. Chem. Soc.* **1982**, *104*, 630–632.
(85) Treadway, J. A.; Loeb, B.; Lopez, R.; Anderson, P. A.; Keene, F. R.; Meyer, T. J. *Inorg. Chem.* **1996**, *35*, 2242–2246.
(86) Noviandri, I.; Brown, K. N.; Fleming, D. S.; Gulyas, P. T.; Lay, P. A.; Masters, A. F.; Phillips, L. *J. Phys. Chem. B* **1999**, *103*, 6713–6722.
(87) Bard, A. J.; Faulkner, L. R. *Electrochemical Methods*, 2nd ed.; John Wiley and Sons, Inc.: New York, 2001.
(88) Howell, S. L.; Gordon, K. C. *J. Phys. Chem. A* **2004**, *108*, 2536–2544.
(89) Lind, S. J.; Gordon, K. C.; Waterland, M. R. *J. Raman Spectrosc.* **2008**, *39*, 1556–1567.
(90) Towrie, M.; Grills, D. C.; Dyer, J.; Weinstein, J. A.; Matousek, P.; Barton, R.; Bailey, P. D.; Subramaniam, N.; Kwok, W. M.; Ma, C.; Phillips, D.; Parker, A. W.; George, M. W. *Appl. Spectrosc.* **2003**, *57*, 367–380.
(91) Brennan, P.; George, M. W.; Jina, O. S.; Long, C.; McKenna, J.; Pryce, M. T.; Sun, X.-Z.; Vuong, K. Q. *Organometallics* **2008**, *27*, 3671–3680.
(92) Frisch, M. J.; Trucks, G. W.; Schlegel, H. B.; Scuseria, G. E.; Robb, M. A.; Cheeseman, J. R.; Scalmani, G.; Barone, V.; Mennucci, B.; Petersson, G. A.; Nakatsuji, H.; Caricato, M.; Li, X.; Hratchian, H. P.; Izmaylov, A. F.; Bloino, J.; Zheng, G.; Sonnenberg, J. L.; Hada, M. E.; Toyota, K.; Fukuda, R.; Hasegawa, J.; Ishida, M.; Nakajima, T.; Honda, Y.; Kitao, O.; Nakai, H.; Vreven, T.; Montgomery, J. A.; Peralta, J. E.; Ogliaro, F.; Bearpark, M.; Heyd, J. J.; Brothers, E.; Kudin, K. N.; Staroverov, V. N.; Kobayashi, R.; Normand, J.; Raghavachari, K.; Rendell, A.; Burant, J. C.; Iyengar, S. S.; Tomasi, J.; Cossi, M.; Rega, N.; Millam, J. M.; Klene, M.; Knox, J. E.; Cross, J. B.; Bakken, V.; Adamo, C.; Jaramillo, J.; Gomperts, R.; Stratmann, R. E.; Yazyev, O.; Austin, A. J.; Cammi, R.; Pomelli, C.; Ochterski, J. W.; Martin, R. L.; Morokuma, K.; Zakrzewski, V. G.; Voth, G. A.; Salvador, P.; Dannenberg, J. J.; Dapprich, S.; Daniels, A. D.; Farkas, Ö.; Foresman, J. B.; Ortiz, J. V.; Cioslowski, J.; Fox, D. J. *Gaussian 09*; Gaussian, Inc.: Wallingford, CT, 2009.
(93) Scott, A. P.; Radom, L. *J. Phys. Chem.* **1996**, *100*, 16502–16513.
(94) Schaftenaar, G.; Noordik, J. H. *J. Comput.-Aided Mol. Des.* **2000**, *14*, 123–134.